Scalable quantum algorithm for meson scattering in a lattice gauge theory

Yahui Chai,* Yibin Guo, and Stefan Kühn
Deutsches Elektronen-Synchrotron DESY, Platanenallee 6, 15738 Zeuthen, Germany

(Received 13 July 2025; revised 28 November 2025; accepted 13 July 2026; published 11 September 2026)

Scattering processes are essential for understanding the structure of matter, yet their real-time dynamics remain challenging to simulate classically. Quantum computers offer a promising path toward efficient simulation of such physical systems. Here, we present a general and scalable framework for simulating meson scattering in lattice gauge theories on digital quantum hardware. Our approach addresses two key challenges: First, we introduce a symmetry-preserving quantum subspace expansion method for constructing high-fidelity meson creation operators across a wide range of coupling and momenta. Second, we design a quantum circuit for meson wave packet preparation using Givens rotations, improving accuracy while reducing circuit depth compared to existing approaches. We demonstrate the method in a $(1+1)$-dimensional $\mathbb{Z}_2$ gauge theory and explore meson scattering dynamics with tensor network simulations. We study both elastic and inelastic scattering and provide a comprehensive characterization of the scattering process in terms of energy transfer, entanglement entropy, and heavier particle production during the dynamics. Our work provides a scalable, nonvariational approach for simulating meson scattering on near-term quantum devices and offers a concrete strategy for probing nonperturbative dynamics in confining gauge theories.

DOI: 10.1103/f93h-rlzy

I. INTRODUCTION

Scattering processes are central to our understanding of the fundamental interactions of matter, as they govern its structure. Particle collision experiments, such as those at the Large Hadron Collider [1], probe theoretical predictions and search for physics beyond the Standard Model. However, simulating the real-time dynamics of scattering events from first principles remains a major challenge. This is because the conventional numerical approach to gauge field theories, which relies on discretizing the Lagrangian on a Euclidean spacetime lattice, is not directly applicable to dynamical processes. While this formulation enables the use of sophisticated Monte Carlo methods and has proven itself highly successful for static observables [2–6], it suffers from the sign problem when applied in Minkowski spacetime required for simulating real-time dynamics [7]. In this case, the probability weights become complex, which prevents an efficient Monte Carlo sampling. As a result, many key aspects such as the intermediate states or the evolution of quantum correlations during the scattering process are poorly understood, as they are also difficult to probe experimentally.

Consequently, there is an ongoing search for alternative methods that can overcome these limitations. In particular, quantum-inspired methods, such as tensor network (TN) states, provide a promising alternative for addressing regimes inaccessible with conventional Monte Carlo methods. While TN methods have already been successfully demonstrated to overcome the sign problem [8–15], they are only efficient in situations where the entanglement is moderate. In out-of-equilibrium processes like particle collisions, entanglement generation can be significant, making dynamical simulations with TN eventually costly [16–18]. In addition, although meson scattering has been simulated with TN in $(1+1)$-dimensional gauge models [14,19], those studies rely on analytical knowledge specific to certain coupling regimes to approximate meson creation operators. A general method to construct such operators across all coupling strengths with high fidelities is still lacking, and the resource requirements remain unclear.

Quantum computing offers a promising path forward for simulating dynamical problems, as its efficiency is not limited by the maximum amount of entanglement. Several proof-of-principle quantum simulations have been realized in simple quantum field theories and lattice gauge models [20–30]. However, implementing scattering processes on a digital quantum computer poses specific challenges, in particular, preparing particle wave packets, which generally involves nonunitary particle creation operators that cannot be directly realized with unitary quantum gates. Reference [26] has addressed this issue for fermion scattering through circuit decompositions based on Givens rotation. For composite particles such as mesons, wave packet preparation is more challenging.

Recent works [25,31–33] have employed variational optimization of quantum circuits to prepare particle wave packets, which have shown strong performance for the ϕ^4 scalar field theory and the Ising model, but remain challenging to extend to gauge theories with fermionic matter, where mesons have a more complex internal structure. In Ref. [34], meson creation operators in gauge theories are constructed via the

*Contact author: yahui.chai@desy.de

variational quantum eigensolver (VQE), reaching high fidelity at low momentum. However, maintaining similar accuracy at high momentum and in the small-mass/weak-coupling regime remains difficult, which is relevant to the high-energy inelastic scattering and for approaching the continuum limit, respectively. Their proposed circuit decomposition for the meson wave packet operator, based on Trotterization and singular value decomposition [35], has a depth scaling as $\mathcal{O}(L^3 N_{\text{Trotter}})$ for general case, with L the lattice size and N_{Trotter} the Trotter steps. Especially on near-term devices, a large circuit depth and Trotter errors can reduce the accuracy of the prepared initial state, which in turn degrades the fidelity of the simulated dynamics.

This work addresses both challenges in a scalable and generalizable way. First, we introduce a symmetry-preserving quantum subspace expansion (QSE) approach for systematically constructing high-fidelity meson creation operators across a wide range of couplings and momenta. Unlike previous variational approaches, our method avoids costly hybrid quantum-classical optimization, can be performed entirely classically using TNs or other Hamiltonian methods, and achieves fidelities above 0.99 even in parameter regimes where VQE-based approaches drop below 0.9. Second, we develop an accurate and resource-efficient circuit decomposition for meson wave packet preparation based on Givens rotations, reducing the circuit depth from $\mathcal{O}(L^3)$ to $\mathcal{O}(L)$ while requiring only nearest- and next-nearest-neighbor connectivity. Although demonstrated here in the $(1+1)$-dimensional $\mathbb{Z}_2$ lattice gauge theory (LGT) [36–38], our methods are general and readily extend to higher-dimensional theories and other gauge groups.

Beyond algorithmic development, we demonstrate the capabilities of our framework through classical simulations of full real-time scattering using matrix product states (MPS), a particular kind of one-dimensional TN. Our results capture both elastic and inelastic processes, including flux string formation and breaking, particle production, energy transfer, and rapid entanglement growth. We provide qualitative diagnostics to analyze these phenomena, offering a concrete strategy for using quantum computing to extract physical insight from real-time scattering. These advances together establish a path toward scalable, interpretable quantum simulations of high-energy dynamics.

This paper is organized as follows. In Sec. II, we introduce the lattice $\mathbb{Z}_2$ gauge theory and its symmetries. In Sec. III, we introduce the QSE construction of meson creation operators. Section IV shows our numerical results, including elastic and inelastic scattering. In Sec. V, we propose an efficient quantum circuit for the preparation of meson wave packets and analyze its resource scaling. Finally, we summarize our results and discuss future research directions in Sec. VI.

II. THE MODEL

In this work, we focus on a $\mathbb{Z}_2$ LGT [36] coupled to staggered fermions [37,38]. It is arguably one of the simplest lattice gauge theories with fermionic matter, as the gauge degrees of freedom on each link correspond to spins with just two states. The Hamiltonian consists of three parts, $H = H_{\text{kin}} + H_{\text{mass}} + H_{\text{el}}$, where the first part corresponds to the kinetic term, the second to the mass term, and the third to the electric energy term. On a lattice with L matter sites, these read

$$\begin{aligned} H_{\text{kin}} &= \frac{1}{2a}\sum_{n=1}^{L}(\xi_n^\dagger Z_{g,n}\xi_{n+1} + \text{H.c.}), \\ H_{\text{mass}} &= m\sum_{n=1}^{L}(-1)^n\xi_n^\dagger\xi_n, \\ H_{\text{el}} &= \varepsilon\sum_{n=1}^{L}X_{g,n}. \end{aligned} \tag{1}$$

In the above expression, the operators $\xi_n^\dagger$ (ξ_n) represent fermionic creation (annihilation) operators on matter site n, and $X_{g,n}$, $Z_{g,n}$ are the usual Pauli matrices acting on the gauge links connecting sites n and $n+1$. Periodic boundary conditions are used to have a good definition of momentum, where site $L+1$ is identified with 1 in the kinetic term. The parameters a, m, and ε correspond to the lattice spacing, the fermion mass, and the coupling, respectively. The gauge degrees of freedom on each link can be described by the eigenstates of the Pauli-X operator $X_{g,n}$, $|+\rangle$, $|-\rangle$ corresponding to electric field values $+1$ and -1. The physical states of the theory have to fulfill Gauss law, $\forall n\ G_n|\psi\rangle = |\psi\rangle$, where

$$G_n = X_{g,n-1}\exp(i\pi Q_n)X_{g,n} \tag{2}$$

and $Q_n = \xi_n^\dagger\xi_n - (1-(-1)^n)/2$ is the staggered fermionic charge. Figure 1(a) provides an illustration of the lattice system. Note that the staggered formulation essentially corresponds to separating the upper (lower) components of the Dirac spinor to even (odd) sites; hence, we focus on even values of L for the rest of the paper. In addition, throughout this work we target the sector with vanishing total charge, $\sum_n Q_n = 0$, which corresponds to half filling, i.e., $\sum_n \xi_n^\dagger\xi_n = L/2$. Besides, we use the dimensionless rescaling of the Hamiltonian aH and set $a = 1$ without loss of generality. As a result, both the fermion mass m and the electric field coupling ε are expressed in units of the lattice spacing and are treated as dimensionless parameters. We vary m and ε to explore different physical regimes of the theory.

The Hamiltonian in Eq. (1) is invariant under charge conjugation. Due to the staggered formulation corresponding to separating the components of the Dirac spinor to different sites, the lattice version of the charge conjugation operator C cannot be defined on a single staggered site, and involves translation by one lattice site [39–41]

$$C\xi_n C^{-1} = (-1)^n\xi_{n+1}^\dagger, \quad CZ_{g,n}C^{-1} = Z_{g,n+1}. \tag{3}$$

Note that C^2 corresponds to a translation by two staggered lattice sites, which leaves the Hamiltonian invariant, too, and allows for the definition of a lattice momentum. Hence, there exists an eigenbasis for the Hamiltonian in which its eigenstates have a well-defined momentum and charge conjugation quantum number: $C|k,c\rangle = ce^{-ika}|k,c\rangle$. Here, $c = \pm 1$ is the charge conjugation quantum number and k is the lattice momentum with possible values $k \in \Lambda = (2\pi/aL)\{-L/2, -L/2+1, \ldots, L/2-1\}$. In the continuum

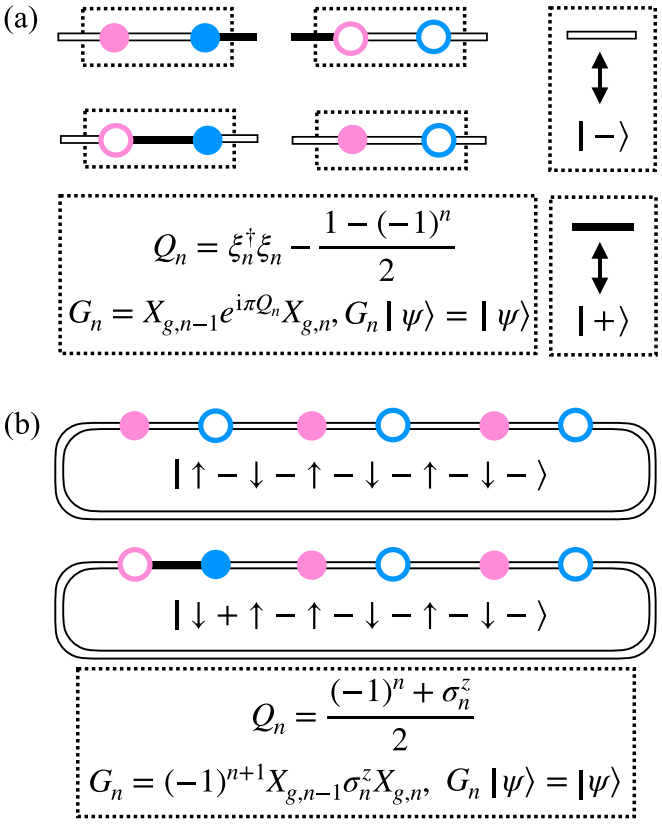

FIG. 1. Illustration of one-dimensional $\mathbb{Z}_2$ LGT. (a) Example configurations satisfying the Gauss law. The pink (blue) circles correspond to odd (even) sites, and solid (empty) circles represent filled (empty) fermions. The fermions are connected by $\mathbb{Z}_2$ gauge field, represented by horizontal lines. The empty (filled) line corresponds to the electric field in the eigenstate $|-\rangle$ ($|+\rangle$), with eigenvalues -1 ($+1$), respectively. Other valid configurations can be obtained by simultaneously flipping all gauge field qubits. (b) The upper part shows the ground state in the strong coupling limit $\varepsilon \to \infty$, where all electric fields take the lowest eigenvalue state, and all odd (even) fermion qubits are spin up (down). A gauge link is connected between the last and first site due to the periodic boundary condition used here. The lower plot shows a meson excitation created by the operator $\xi_1 Z_{g,1} \xi_2^\dagger$, which annihilates a fermion at site 1 (thereby effectively creating an antifermion) and creates a fermion at site 2, resulting in an antifermion-fermion pair connected by an electric flux string to satisfy the Gauss law.

limit, $ka \to 0$, C will reduce to the usual charge conjugation operator.

In the well-studied Schwinger model, the two stable particles are the vector and the scalar meson, which are characterized by their charge conjugation number [42,43]. We observe the same behavior for the lattice $\mathbb{Z}_2$ gauge theory in our numerical results: The ground state lies in the charge conjugation sector $c = +1$, and the first zero-momentum excitation is directly above the ground states with $c = -1$; hence, we refer to it as the vector meson. Similar to Ref. [43], we observe the second zero-momentum excitation having $c = +1$, which we refer to as the scalar meson in analogy to the Schwinger model.

In order to simulate the model on a quantum computer, we map the fermionic degrees of freedom to spins using a Jordan-Wigner transformation (JWT)

$$\xi_n^\dagger = \prod_{l<n} \left(-i\sigma_l^z\right)\sigma_n^+, \quad \xi_n = \prod_{l<n} \left(i\sigma_l^z\right)\sigma_n^-, \tag{4}$$

where $\sigma_n^\pm = (\sigma_n^x \pm i\sigma_n^y)$, and we use σ_n^a, $a = x, y, z$, for Pauli matrices acting on the matter sites to explicitly distinguish them from the gauge degrees of freedom. The resulting spin Hamiltonian reads

$$\begin{aligned} H = &-\frac{i}{2a}\sum_{n=1}^{L-1}(\sigma_n^+ Z_{g,n}\sigma_{n+1}^- - \text{H.c.}) \\ &+ \frac{1}{2a}\left(\prod_{l<L}\left(-i\sigma_l^z\right)\sigma_L^+ Z_{g,L}\sigma_1^- + \text{H.c.}\right) \\ &+ \frac{m}{2}\sum_{n=1}^{L}(-1)^n\sigma_n^z + \varepsilon\sum_{n=1}^{L} X_{g,n}, \end{aligned} \tag{5}$$

where the second line arises due to the periodic boundary conditions and we have omitted the constant $\sum_{n=1}^{L}(-1)^n m/2$ in mass term, as it evaluates to zero for even values of L used in this work. The Gauss law in spin language corresponds to

$$G_n = (-1)^{n+1} X_{g,n-1}\sigma_n^z X_{g,n}. \tag{6}$$

Consequently, a total of $N = 2L$ qubits are required to represent both the fermionic matter fields and the gauge degrees of freedom in a system comprising L sites.

III. MESON OPERATOR CONSTRUCTION

In order to be able to create meson wave packets, we first need to find operators that allow us to create an interacting meson on top of a given state. Constructing accurate meson creation operators is particularly challenging, and several approaches have been suggested. Reference [32] proposes preparing a wave packet based on a W state and optimizing it using a translationally invariant quantum circuit to minimize energy, aiming to generate the lightest particle in the interacting theory. Their approach performs well for the Ising model and the ϕ^4 scalar field theory. Applied to the Schwinger model, the observed fidelities are lower, likely due to the more complex internal structure of the mesons.

Reference [34] uses VQE to optimize ansatz parameters for constructing the lowest-energy eigenstate at fixed momentum in a $(1+1)$-dimensional $\mathbb{Z}_2$ LGT as well as the Schwinger model. This method shows high fidelity for small systems ($L \leqslant 10$) in the strong-coupling or large-mass regime, but maintaining high fidelity in the small-mass and weak-coupling regime, especially for high momenta, seems challenging. Moreover, VQE can be difficult to scale in practice due to the generally large number of measurements required and hardware imperfections that can degrade the tractability of this procedure, particularly as the system size increases [44–46].

In this work, we instead propose to use QSE [47–50] to determine operators that allow us to create a meson on top of the ground state. We demonstrate that this approach is able to produce meson states in the $\mathbb{Z}_2$ LGT with high fidelity

over a wide range of system sizes, momenta, and Hamiltonian parameters.

In the sector of vanishing total charge, because of confinement in the $\mathbb{Z}_2$ gauge theory [27], the mesons represent bound states of a fermion and an antifermion. This picture becomes more clear in the strong coupling limit, $\varepsilon \to \infty$, for which the contribution of the kinetic and the mass term in the Hamiltonian can be omitted. The ground state in this limit is given by

$$|\Omega_\infty\rangle = |1\rangle|-\rangle|0\rangle|-\rangle|1\rangle\cdots|-\rangle|0\rangle|-\rangle, \tag{7}$$

where all gauge links are arranged in the configuration minimizing the electric energy, and the odd (even) sites are occupied (empty) due to the fact that the staggered charge has to vanish to fulfill the Gauss law in Eq. (2) for this electric field configuration. Note that this state also minimizes the mass energy in the absence of the kinetic term. The excited states in this limit correspond to fermion-antifermion pairs between nearest neighbors, which must be connected by a flux tube to satisfy the Gauss law [cf. Fig. 1(b)]. These excitations can be represented as

$$|k=0, c=-1\rangle_b = \sum_n (\xi_n^\dagger Z_{g,n}\xi_{n+1} - \text{H.c.})|\Omega_\infty\rangle, \tag{8}$$

where the subscript b denotes a meson state, $k=0$ represents the meson's momentum, and $c=-1$ specifies the charge conjugation of this meson. In contrast, in the weak coupling region, a meson state can be approximated as the product of zero-momentum fermions and antifermions [19]. In this situation, the meson has a looser structure and the fermion-antifermion pairs are connected by longer flux tubes compared to the strong coupling limit. In general, we expect the operator creating a meson with momentum k and charge conjugation c to have the form

$$b_{k,c}^\dagger = \sum_{n,l=1}^{L} a_{n,l}^{(k,c)}\, \xi_n^\dagger W_{n,l}\xi_l \equiv \sum_I a_I^{(k,c)}\, M_I, \tag{9}$$

where $a_{n,l}^{(k,c)}$ are complex coefficients. To simplify the equations for the QSE later on, we define a multi-index $I=(n,l)$ and the shorthand operator $M_I = \xi_n^\dagger W_{n,l}\xi_l$. The operator $W_{n,l}$ is the Wilson line connecting the fermionic operators at sites n and l. Since we consider a periodic boundary condition, there are two possible paths to connect these two sites, where it is energetically favorable to choose the shorter one to have a lower electric field energy. For $n<l$, the Wilson line is defined as

$$W_{n,l} = \begin{cases} \prod_{r=n}^{l-1} Z_{g,r}, & l-n \leqslant \frac{L}{2}, \\ \left(\prod_{r=1}^{n-1} Z_{g,r}\right)\left(\prod_{r=l}^{L} Z_{g,r}\right), & l-n \geqslant \frac{L}{2}, \end{cases} \tag{10}$$

and similarly for the case $n>l$. Note that the Wilson line only involves Pauli-Z operators acting on the links and, thus, is self-adjoint.

With appropriate choice of coefficients $a_I^{(k,c)}$, the operator $b_{k,c}^\dagger$ will excite a proper meson state from the ground state $|\Omega\rangle$,

$$|k,c\rangle_b = b_{k,c}^\dagger|\Omega\rangle = \sum_I a_I^{(k,c)}\, M_I|\Omega\rangle, \tag{11}$$

which is an eigenstate of both the Hamiltonian and the charge conjugation operator

$$H|k,c\rangle_b = E|k,c\rangle_b, \quad C|k,c\rangle_b = ce^{ik}|k,c\rangle_b. \tag{12}$$

To find the optimal coefficients $\vec{a}^{(k,c)} = \{a_{1,1}^{(k,c)}, a_{1,2}^{(k,c)}, \ldots\}$, we use a subspace expansion method (see Appendix A). To this end, we solve the generalized eigenvalue problem

$$(\mathcal{H}+\mathcal{C})\vec{a}^{(k,c)} = \lambda\, \mathcal{S}\vec{a}^{(k,c)}, \tag{13}$$

on the subspace

$$\{M_I|\Omega\rangle | I \in \{1,2,\ldots,L\}^2\}. \tag{14}$$

In Eq. (13), the generalized eigenvalues are given by $\lambda = E + ce^{-ika}$ and the matrices $\mathcal{H}$, $\mathcal{C}$, and $\mathcal{S}$ have the entries

$$\begin{aligned} \mathcal{H}_{I,J} &= \langle\Omega|M_I^\dagger H M_J|\Omega\rangle, \\ \mathcal{C}_{I,J} &= \langle\Omega|M_I^\dagger C M_J|\Omega\rangle, \\ \mathcal{S}_{I,J} &= \langle\Omega|M_I^\dagger M_J|\Omega\rangle. \end{aligned} \tag{15}$$

The above matrix elements are expectation values of operators. Here, we choose to compute them with MPS [51], but any other Hamiltonian method that allows for computing these matrix elements is equally applicable. In particular, on quantum hardware, expectation values of Hermitian operators can be measured directly, while the non-Hermitian operators appearing above can be decomposed into linear combinations of Pauli operators. The desired matrix elements are then obtained by combining the individually measured contributions.

In addition, the meson annihilation operator $b_{k,c}$ should satisfy $b_{k,c}|\Omega\rangle = 0$. This condition can be ensured by adding an additional term to the QSE equations; otherwise, the solution of Eq. (13) may yield coefficients contaminated by unwanted annihilation operators. A simple example is operators like $\tilde{b}_{k,c}^\dagger = b_{k,c}^\dagger + b_{k',c'}$, where $b_{k',c'}$ is an arbitrary meson annihilation operator. While $\tilde{b}_{k,c}^\dagger$ will still excite eigenstates of H and C, it will generally not fulfill the condition $\tilde{b}_{k,c}|\Omega\rangle = b_{k',c'}^\dagger|\Omega\rangle \neq 0$. Hence, an extra term has to be added to enforce that the norm $\mathcal{N}_\mathcal{Z} \equiv \langle\Omega|b_{k,c}^\dagger b_{k,c}|\Omega\rangle$ is zero, as explained in Appendix A,

$$\mathcal{Z}_{I,J} = \langle\Omega|M_J M_I^\dagger|\Omega\rangle. \tag{16}$$

The final QSE equation including all terms to satisfy all requirements reads

$$(\mathcal{H}+\mathcal{C}+\mathcal{Z})\vec{a}^{(k,c)} = \lambda\, \mathcal{S}\vec{a}^{(k,c)}, \tag{17}$$

where now $\lambda = E + ce^{-ika} + \mathcal{N}_\mathcal{Z}$. After normalizing the coefficients to satisfy $\mathcal{N}_\mathcal{S} \equiv \vec{a}^{(k,c)\dagger}\mathcal{S}\vec{a}^{(k,c)} = 1$, the physical quantities can be extracted separately by

$$\begin{aligned} E &= \vec{a}^{(k,c)\dagger}\mathcal{H}\vec{a}^{(k,c)}, \\ ce^{-ik} &= \vec{a}^{(k,c)\dagger}\mathcal{C}\vec{a}^{(k,c)}, \\ \mathcal{N}_\mathcal{Z} &= \vec{a}^{(k,c)\dagger}\mathcal{Z}\vec{a}^{(k,c)}. \end{aligned} \tag{18}$$

We select the vectors $\vec{a}^{(k,c)}$ with lowest values of $E+\mathcal{N}_\mathcal{Z}$ to ensure both low energy and minimal annihilation contribution. In our simulations, we typically find values of $\mathcal{N}_\mathcal{Z} \sim 0.001$ for $m=0.1, \varepsilon=1.0$, and ~ 0.01 for $m=0.1, \varepsilon=0.2$. For $k \neq 0$, states with momentum k and $-k$ have the same energy

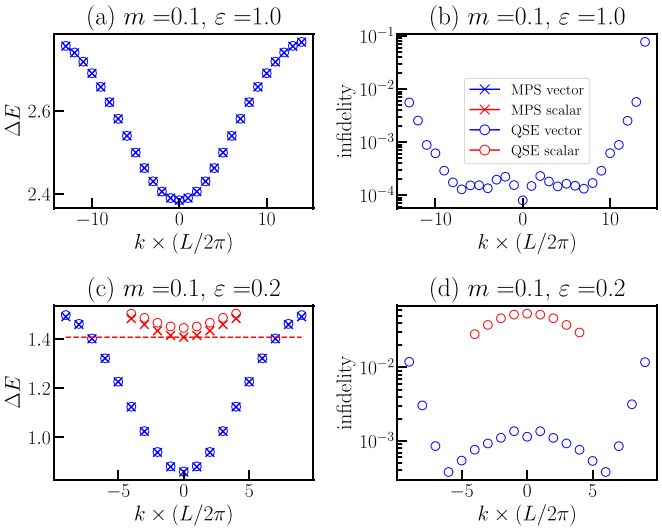

FIG. 2. Energy difference of the excited states with respect to the ground state for $L = 30$, $m = 0.1$, and $\varepsilon = 1.0$ [panel (a)], and 0.2 [panel (c)]. The blue (red) markers correspond to the vector (scalar) meson excitations, circles indicate the energies obtained by QSE, and crosses indicate those from MPS simulations. The x axis is the corresponding integer lattice momenta k in units of $L/2\pi$. Panels (b) and (d) show the corresponding infidelity between the states obtained by our QSE approach and the excited states obtained directly from the MPS simulation. The red dashed horizontal line in panel (c) indicates the mass of the scalar meson obtained from the MPS approach.

and can be distinguished by the eigenvalue of the charge conjugation operator: ce^{-ik}. We note that when only a specific momentum mode is targeted, the operator pool in Eq. (14) can be substantially reduced by exploiting translation invariance, as detailed in Appendix G.

In order to demonstrate that our approach produces high-fidelity mesonic excitations, we use MPS and first compute the ground state of the Hamiltonian using standard variational methods [52]. To obtain the excited states, we proceed in two ways. First, we use again standard variational MPS methods to compute the excited states of the model. Second, we create the subspace from Eq. (14) explicitly by applying the meson operators on the MPS ground state. This allows us to construct the matrices in Eq. (17) and to solve the generalized eigenvalue problem and to compare the results from our method to the MPS data. In Fig. 2, we show the energy difference ΔE with respect to the ground state and the infidelity for the lowest-lying 28 excited states obtained from both methods for a system with $L = 30$, $m = 0.1$, and various values of ε. Note that the data for $k = 0$ correspond to the meson's mass in units of the lattice spacing. Focusing on strong coupling, $\varepsilon = 1.0$, Fig. 2(a) shows that the first 28 excitations are vector mesons, and, as expected, the ones with $k \neq 0$ appear in pairs having the same absolute value of the momentum due to translation invariance. The energies obtained from our QSE method are in excellent agreement with the MPS solution. Looking at infidelities in Fig. 2(b), we observe that the meson excitations constructed using our subspace expansion approach are close to the MPS solution and for the low-lying states we obtain fidelities exceeding or approaching 99.9%. Only for excitations

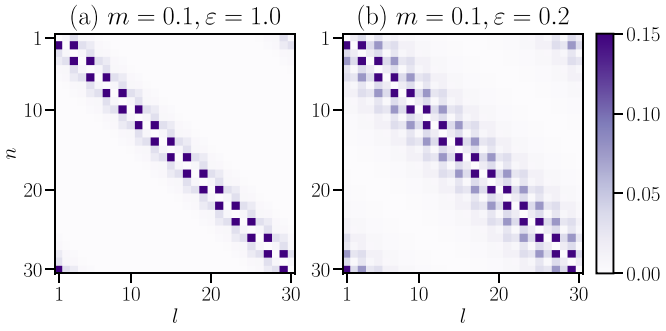

FIG. 3. Distribution of vector meson's coefficients for $k = 0$ at (a) $\varepsilon = 1.0$ and (b) $\varepsilon = 0.2$. The color bar represents the absolute value of coefficients, $|a^{0,-1}_{n,l}|$.

with large absolute momentum the accuracy drops slightly, and for almost all states we have infidelities smaller than 1%.

At smaller values of the coupling, $\varepsilon = 0.2$, we see a similar vector meson branch as for the larger coupling, but the meson mass is significantly lighter than in the previous case. In addition, also scalar particles appear within the first 28 excited states [see Fig. 2(c)]. The fidelities for the vector meson excitations obtained from QSE show a similar behavior as for the larger value of the coupling, and most of them are above 99%. For the scalar mesons, the fidelity is slightly worse than for the vector branch, but still does not drop below 94.6% despite us choosing the simplest mesonic operators in the ansatz in Eq. (9).

Note that our approach is systematically improvable. While we obtain very high fidelities by considering only pairs of creation and annihilation operators in Eq. (9) in the regimes we study, it is straightforward to include more complex fermionic operators such as four-fermion interactions in the ansatz for the meson creation operators. Including these operators can further enhance the fidelity of scalar mesons, potentially bringing it to the same level as for the vector branch. This allows for systematically enlarging the subspace, thereby providing a way to improve the accuracy of the results. In addition, Appendix B contains more detailed numerical benchmarks demonstrating the high fidelity of the QSE method across different parameter regimes, as well as its scalability to system sizes of up to 60 sites.

Furthermore, the coefficients obtained from QSE provide insight into the internal structure of the meson at different coupling strengths. To illustrate this, Fig. 3 shows the distribution of vector meson's coefficients $a^{0,-1}_{n,l}$ obtained from Eq. (17). Looking at the vector meson at $k = 0$ for a large coupling, $\varepsilon = 1.0$, Fig. 3(a) reveals that the coefficients for operators acting on nearest-neighbor matter sites dominate, i.e., $a^{0,-1}_{n,n-1}$ and $a^{0,-1}_{n,n+1}$. This indicates the meson is primarily composed of fermion-antifermion pairs connected by one excited electric link, as one might expect from the strong coupling picture in Fig. 1. In contrast, at a weaker coupling of $\varepsilon = 0.2$ the vector meson exhibits a looser structure, allowing the fermion-antifermion pairs to separate further and be connected by longer flux strings containing more links. This results in more coefficients having significant values, as Fig. 3(b) shows.

IV. MESON SCATTERING

Using the meson operators constructed in the previous section, we can now build operators creating vector meson wave packets. To this end, we define

$$B^\dagger_{\bar{k},\bar{x}} = \sum_{k\in\Lambda^*} \phi(k)_{\bar{k},\bar{x}} b^\dagger_{k,-1} = \sum_{k\in\Lambda^*}\sum_{nl} \phi(k)_{\bar{k},\bar{x}} a^{k,-1}_{nl} \xi^\dagger_n W_{n,l}\xi_l,$$
$$\phi_{\bar{k},\bar{x}}(k) = \frac{1}{\sqrt{\mathcal{N}_\phi}} e^{-ik\bar{x}} e^{-(k-\bar{k})^2/(4\sigma_k^2)}, \tag{19}$$

where $\phi_{\bar{k},\bar{x}}(k)$ is a complex Gaussian distribution, $\bar{x}$, $\bar{k}$ represent the mean values of the wave packet's position and momentum, and σ_k corresponds to its width in momentum space. Moreover, $\mathcal{N}_\phi = \sum_k |\phi(k)|^2$ is the normalization factor of the Gaussian distribution. Note that Λ^* does not correspond to the entire momentum space but rather to the momenta $k \in \Lambda$ that appear when solving Eq. (17). For example, for $\varepsilon = 0.2$ shown in Fig. 2(c), $\Lambda^* = (2\pi/L) \times \{-9, -8, \ldots, 9\}$ for the vector meson, and $\Lambda^* = (2\pi/L) \times \{-4, -3, \ldots, 4\}$ for scalar meson. Similarly, for example, with $\varepsilon = 1.0$, for which only the vector meson appears [cf. Fig. 2(a)], one obtains $\Lambda^* = (2\pi/L) \times \{-13, -12, \ldots, 14\}$. The restriction of the momentum modes in Eq. (19) will result in a wave packet that is not perfectly Gaussian. Due to the wave packet's localization in momentum space, the truncation error introduced by a finite momentum basis Λ^* remains small as long as the central momentum $\bar{k}$ is far away from boundaries of Λ^*. In such cases, momenta near the cutoff are naturally suppressed by the Gaussian distribution, and the resulting wave packet remains well defined. However, for wave packets with higher momenta, e.g., $|\bar{k}| = (2\pi/L) \times 8$ with $(m, \varepsilon) = (0.1, 0.2)$, the momentum cutoff will introduce noticeable truncation effects. This leads to an effectively narrower wave packet in momentum space and a broader one in position space. These effects can be mitigated by including more excited states in the subspace or using larger system sizes, which offer finer momentum resolution for defining narrow wave packets and enough spatial extent to separate broad wave packets.

To quantify the truncation effects systematically, we also tested case $(m, \varepsilon) = (0.2, 0.2)$ and included two more excited states, yielding a larger momentum window $\Lambda^* = (2\pi/L) \times \{-10, -9, \ldots, 10\}$ [53]. This extended window essentially eliminates the momentum truncation error for $(m, \varepsilon) = (0.2, 0.2)$. As detailed in Appendix F, the scattering results obtained with the original truncation $|k| \leqslant 9 \times (2\pi/L)$ and the extended truncation $|k| \leqslant 10 \times (2\pi/L)$ are fully consistent. We therefore conclude that the momentum truncation used for $(m, \varepsilon) = (0.1, 0.2)$ does not affect the physical conclusions of this work.

Using the operator defined in Eq. (19), one can prepare an initial state with two vector mesons to study their scattering processes. More specifically, for time $t = 0$, the initial state we consider is given by

$$|\psi(t=0)\rangle = B^\dagger_{\bar{k},\bar{x}_1} B^\dagger_{-\bar{k},\bar{x}_2} |\Omega\rangle, \tag{20}$$

where the two wave packets are initially localized at $\bar{x}_1$ and $\bar{x}_2$, with momentum of equal magnitude $|\bar{k}|$ but opposite signs and the identical width σ_k. The time evolution $|\psi(t)\rangle = e^{-iHt}|\psi(0)\rangle$ can be computed with standard methods, e.g., using Trotterization.

To demonstrate that our method enables the preparation of wave packets and the investigation of scattering processes, we examine the collision of two mesons. Specifically, we consider a system with $L = 30$, which corresponds to $N = 60$ qubits, and we choose $\bar{x}_1 = 8$ and $\bar{x}_2 = 23$ and a width $\sigma_k = 2\pi/L$. To compute the time evolution, we use time-evolution block decimation (TEBD) with a second-order Trotter step, as detailed in Appendix E. In order to characterize the scattering process, we monitor various observables. In particular, we compute the site-resolved flux configuration, $\langle\psi(t)|X_{g,n}|\psi(t)\rangle$, and measure the staggered fermion density operator χ_n on each site [34]

$$\chi_n = \begin{cases} 1 - \xi^\dagger_n \xi_n, & n \in \text{odd}, \\ \xi^\dagger_n \xi_n, & n \in \text{even}. \end{cases} \tag{21}$$

To gain insight into the energy transfer during the scattering process, we track the time-dependent contributions of the kinetic, mass, and electric components of the Hamiltonian. More specifically, we monitor

$$\delta E_B(t) = \langle\psi(t)|H_B|\psi(t)\rangle - \langle\psi(0)|H_B|\psi(0)\rangle, \tag{22}$$

where H_B is one of the terms in Eq. (1), and the initial value at $t = 0$ is subtracted to clearly show the variation of each energy component. In addition, we also monitor the number of vector and scalar mesons throughout the collision by computing

$$\rho_c = \sum_{k\in\Lambda^*} \langle\psi(t)|b^\dagger_{k,c} b_{k,c}|\psi(t)\rangle, \tag{23}$$

where $c = -1$ $(+1)$ corresponds to the vector (scalar) mesons. This allows us to draw conclusions if vector mesons are annihilated during the scattering event at the expense of creating scalar mesons. Furthermore, at the collision point, two localized mesons can merge due to fermion-antifermion annihilation, resulting in an extended meson connected by a longer flux string. To probe this process and the subsequent string breaking [27], we calculate the probability P_l of observing a single flux string of length l at time t, given by

$$P_l = \sum_{n=1}^{L-l} |\langle\psi(t)|\xi^\dagger_n W_{n,n+l}\xi_{n+l}|\Omega\rangle|^2 + \sum_{n=l+1}^{L} |\langle\psi(t)|\xi^\dagger_n W_{n,n-l}\xi_{n-l}|\Omega\rangle|^2, \tag{24}$$

where $l \in \{1, \ldots, L/2\}$ is restricted due to the periodic boundary conditions, consistent with Eq. (10). Note that we include both strings between fermion and antifermion (first line) as well as between antifermion and fermion (second line).

First, we study the case of $m = 0.1$, $\varepsilon = 1.0$, for which we did not observe any scalar mesons in the low-lying spectrum [cf. Fig. 2(a)]. Figure 4 displays our results for the evolution of two vector meson wave packets with opposite momenta where $\bar{k} = 6 \times (2\pi/L)$. Figure 4(a) shows the site-resolved staggered fermion density over time, where we subtract the fermion density of the ground state and consider $\Delta\langle\chi_n\rangle = \langle\psi(t)|\chi_n|\psi(t)\rangle - \langle\Omega|\chi_n|\Omega\rangle$. As indicated by

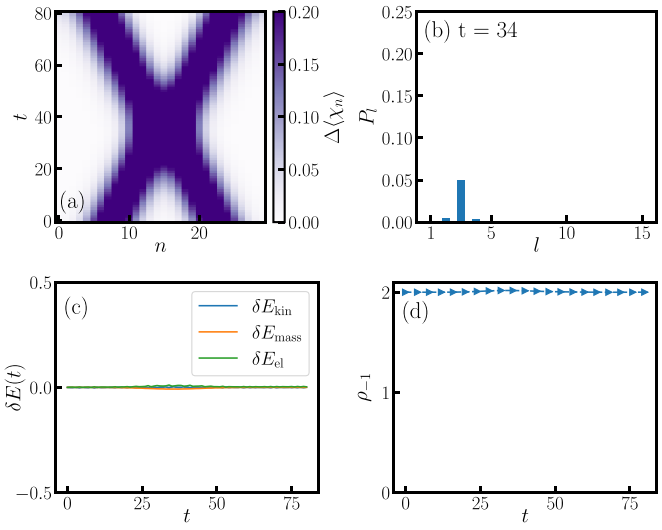

FIG. 4. Time evolution of two meson wave packets with $m = 0.1$, $\varepsilon = 1.0$, and momentum $\bar{k}_1 = 6 \times (2\pi/L)$. (a) Site-resolved staggered fermion density during the evolution. (b) Probability of having a single flux string with length l at time $t = 34$, which is around the collision of the two wave packets. (c) Change of kinetic, mass, and electric field energies over time. (d) Vector meson number ρ_{-1} over every four time steps.

the fermion density, the two vector mesons propagate toward each other during the time evolution and eventually collide. The collision appears to be elastic, as there is no evidence of particle production in $\Delta\langle\chi_n\rangle$. This is further corroborated by the individual energy contributions in Fig. 4(c) and the vector meson number in Fig. 4(d). In particular, we observe that the individual parts of the Hamiltonian are almost conserved, and ρ_{-1} has a value close to 2 throughout the entire evolution, providing evidence that no particles are produced. In addition, we monitor the probability P_l of forming a single flux string of length l [as defined in Eq. (24)]. At the beginning, the system has two separate flux strings coming from the two mesons, resulting in $P_l = 0$. As the two mesons approach each other, these two strings merge into a single longer string, leading to a peak in P_l around $l = 3$ at $t = 34$ close to the collision, as Fig. 4(b) shows. After the collision, the flux string breaks, and P_l returns to zero, indicating the hadronization to two separated mesons. The details of this string formation and breaking process can be found in Appendix D.

Second, we investigate the case of a smaller coupling, $m = 0.1$, $\varepsilon = 0.2$, for which we see a scalar meson in the low-energy spectrum [see Fig. 2(c)]. Figure 5 shows the meson scattering process for various values of the momentum of the initial wave packets. In addition to the previous case, we also display the site-resolved electric field over time, where we again subtract the values of the ground state and consider $\Delta\langle X_{g,n}\rangle = \langle\psi(t)|X_{g,n}|\psi(t)\rangle - \langle\Omega|X_{g,n}|\Omega\rangle$. Focusing on the case of small momentum $\bar{k} = 4 \times (2\pi/L)$ first (cf. left column of Fig. 5), we observe indications for inelastic scattering. While there are no direct signs for the generation of particles, the internal structure of the mesons changes during the collision. In particular, at the collision point around $t = 20$, the staggered fermion density in Fig. 5(a) shows a dip in the center of the system, which is accompanied by an increase in the electric field [cf. Fig. 5(e)]. This indicates again fermion-antifermion annihilation and the formation of strings, which can be seen in Fig. 5(i), showing noticeable probabilities for a single flux tube of length $l > 1$. Compared to the case of larger coupling, longer strings are generated because of the smaller electric field energy contribution per link. After $t = 20$, the string breaks again and fermions are regenerated, which subsequently hadronize to two outgoing vector mesons (see Appendix D for details). This observation is also confirmed by the different energy contributions in Fig. 5(m) and the vector meson number in Fig. 5(q). Around $t = 20$, both mass and kinetic energy decrease and are transformed into electric field energy. The formation of the string results in a significant reduction of the vector meson number, which is subsequently restored. Moreover, the scalar meson number ρ_1 stays close to 0 over the entire time and only shows a slight increase as the two vector mesons approach each other, thus confirming that essentially no scalar mesons are produced. The slight increase of ρ_1 after $t = 40$ can be attributed to the periodic boundary conditions, which cause the two vector mesons to approach each other again.

Increasing the momentum to $\bar{k} = 6 \times (2\pi/L)$ (cf. second column of Fig. 5), we observe a fairly similar picture. However, due to the higher momentum, the resulting strings can extend to longer lengths, which can be observed in Fig. 5(f) around $t = 20$–30 in form of an extended spatial region with high electric flux, and in Fig. 5(j) showing a dominating contribution for $l = 7$. As displayed in Fig. 5(n), during the formation of the strings, the kinetic energy decreases and the electric field energy increases since longer flux tubes require higher energy. After the kinetic energy is exhausted, the fermion-antifermion pairs at the string's end points are pulled back toward each other and collide again. From $t = 40$ onward, there are some fermion-antifermion pairs remaining connected with flux tubes in the middle of the system (see also Appendix D), but most of the fermions hadronize to vector mesons going out. According to Fig. 5(r), there is a signal that some scalar mesons are generated during the collision. However, ρ_1 decreases again significantly after $t = 40$, indicating that no stable scalar mesons are formed.

Studying an even larger momentum of $\bar{k} = 8 \times (2\pi/L)$, one enters a regime where the vector meson has a higher energy than a scalar meson with $k = 0$, as shown by the dashed line in Fig. 2(c). Thus, we expect that stable scalar mesons can form during the scattering process in this case. Looking at the fermion density and the electric field in Figs. 5(c) and 5(g), we indeed observe two outgoing particles with a slower velocity and stronger electric field after the collision. Contrary to the previous case, during the collision we do not observe a significant probability for a single flux string in Fig. 5(k) and the electric field at the collision point is significantly smaller than before. Focusing on the different energy contributions in Fig. 5(o), we see that the kinetic energy initially decreases and stabilizes at a value lower than the initial one after the collision, which is consistent with the smaller velocity of the outgoing particles. Most of this kinetic energy is transferred to the electric field energy, as the increase in $\delta E_{\rm el}(t)$ shows. Besides, we observe a clear decrease of the vector meson number ρ_{-1} from an initial value of 2 to 1 after the collision,

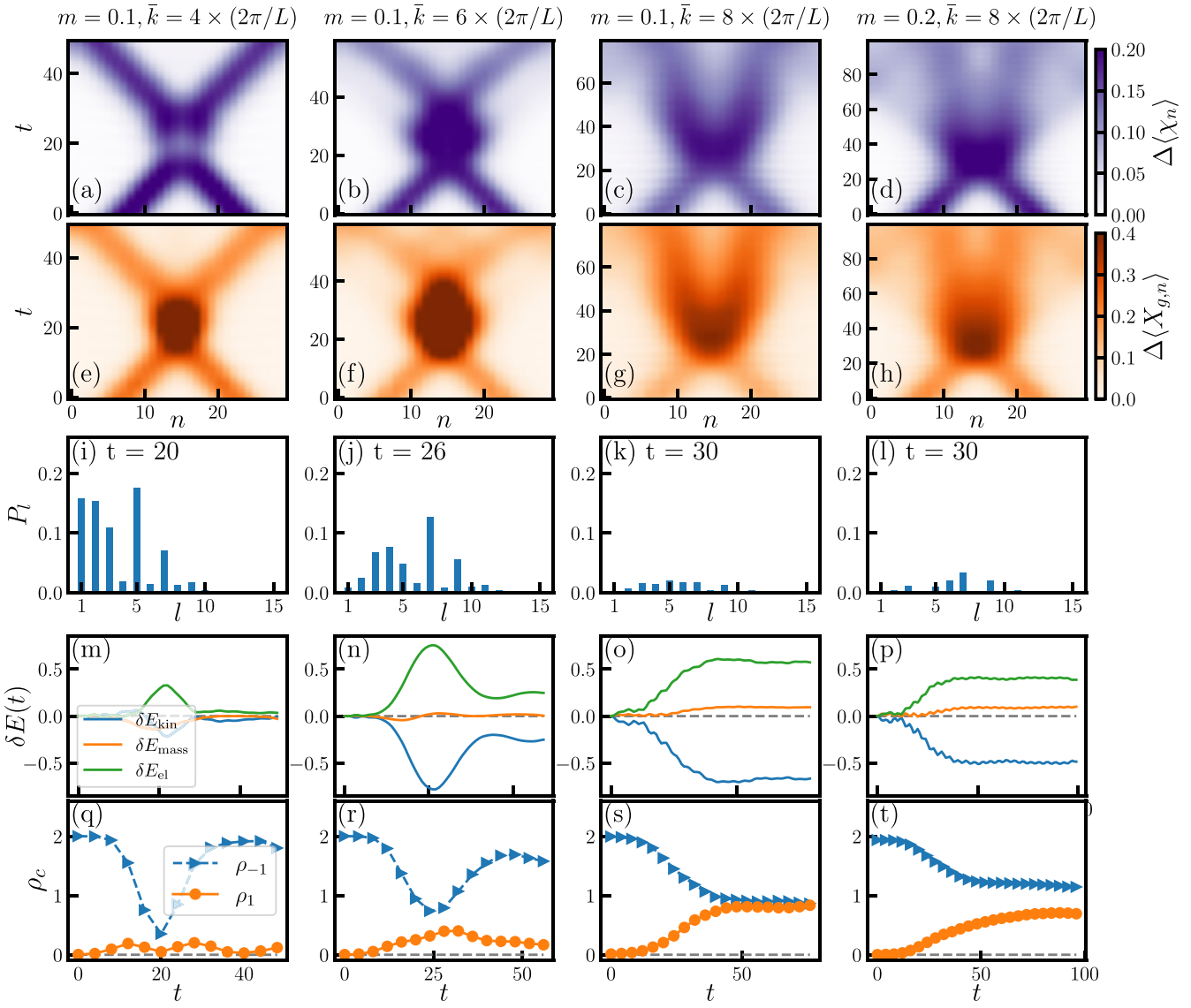

FIG. 5. Scattering process between two vector meson wave packets with $\varepsilon = 0.2$. Each column corresponds to different masses m and initial momenta $\bar{k}$, as indicated in the title of each column. The first row shows the staggered fermion density; the second row shows the electric field density. Both are plotted as functions of position n (x axis) and time t (y axis), and share the same x axis. The third row shows the probability of observing a single flux string at the collision point, plotted vs the string length l (x axis), with probability defined in Eq. (24). The fourth row displays the time evolution of the kinetic, mass, and electric energy contributions, while the fifth row shows the number of vector and scalar mesons over time. The x axis in the fourth and fifth rows is time t.

where simultaneously the scalar meson number ρ_1 increases and also stabilizes around a value of 1 after the collision. This indicates that there are scalar mesons generated after the collision, while there is still a significant probability for two outgoing vector mesons. However, the staggered fermion density and the electric field density only display two fairly broad trajectories after the collision. This could be an effect of the resulting wave packets being spread out rather than remaining localized, and thus they overlap. The corresponding time-resolved string probabilities are shown in Appendix D.

To obtain a clearer picture of the formation of scalar mesons, we repeat the simulation for $\bar{k} = 8 \times (2\pi/L)$ but we use a slightly larger mass of $m = 0.2$. This should result in the scalar mesons being heavier, thus having a smaller velocity after the collision and separating them better from the vector mesons. The results for this case are shown in the right column of Fig. 5. While the data are qualitatively similar to those of the smaller mass $m = 0.1$, the staggered fermion density and also the electric field now show indications for four outgoing trajectories [see Figs. 5(d) and 5(h)]. Given energy conservation, these particles should consist of two heavier scalar mesons with low velocity and two vector mesons with higher velocity. While in this case the scalar meson number ρ_1 remains a little lower [see Fig. 5(t)], the separation in velocity provides clearer evidence for the formation of stable scalar mesons in the scattering process. The corresponding string-formation and breaking dynamics are shown in Appendix D.

Finally, we evaluate the bipartite entanglement entropy between the subsystems $\mathcal{L} = \{n \leqslant L/2\}$ and $\mathcal{R} = \{n > L/2\}$. Specifically, we calculate the von Neumann entropy $S(t) =$

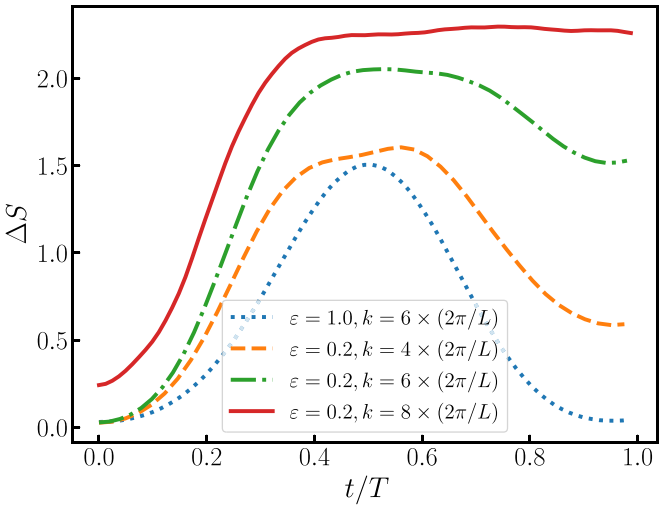

FIG. 6. Bipartite entanglement entropy for both elastic and inelastic scattering processes with $m = 0.1$. Time is measured in units of the total evolution time T to allow for comparing different scattering processes in a consistent manner. The final time T is selected such that the particles have sufficient time to propagate after the collision, but short enough to prevent them from reaching the boundaries of the system. This choice is made to prevent an artificial increase in entanglement entropy that would result from the wave packets splitting as they cross the system's boundary. The blue dotted line corresponds to the elastic scattering with $\varepsilon = 1.0, \bar{k} = 6 \times (2\pi/L)$, and $T = 70$. The orange dashed, green dash-dotted, and red solid lines are associated with the inelastic scattering with $\varepsilon = 0.2$, for momentum $\bar{k} = 4 \times (2\pi/L), 6 \times (2\pi/L), 8 \times (2\pi/L)$ and $T = 40$, 50, and 80, respectively.

$-\mathrm{tr}[\tilde{\rho}(t)\log_2\tilde{\rho}(t)]$, where $\tilde{\rho}(t)$ is the reduced density matrix of one subsystem at time t, then subtract the vacuum contribution to obtain $\Delta S(t)$. We consider $m = 0.1$ and both elastic scattering with $\varepsilon = 1.0$ as in Fig. 4, and the inelastic scattering processes with $\varepsilon = 0.2$ as shown in the first three columns of Fig. 5. For these processes, the evolution of the bipartition entropy is shown in Fig. 6. For the elastic case (blue dotted line), the entropy increases as the two mesons propagate toward the center and decreases after the collision, eventually resulting in nearly zero excess entropy relative to the vacuum. In contrast, for the inelastic scattering processes with $\varepsilon = 0.2$, the peak in entropy at the collision point is larger, and also the final value after the scattering process is higher, especially for a high momentum of $\bar{k} = 8 \times (2\pi/L)$. This indicates that inelastic scattering will be more challenging for the numerical methods based on TN. Specifically, in our MPS simulations we see that for reaching a given precision, the maximal size of the matrices required is around 55 for the elastic case (cf. blue dotted line in Fig. 6), whereas during the simulation, it reaches around 1000 for the inelastic scattering associated with the red solid line in Fig. 6.

V. PREPARING WAVE PACKETS ON A DIGITAL QUANTUM COMPUTER

In the previous sections, we discussed how to construct proper operators for creating meson wave packets and investigated scattering processes using MPS simulations. Our results show that inelastic scattering processes can be challenging to simulate classically with TN, motivating the exploration of quantum computing as a promising alternative for these regimes. As outlined in Sec. IV, simulating the scattering process on a quantum computer requires first preparing the initial state comprising particle wave packets, followed by applying time evolution. The quantum circuit for time evolution can be implemented using Trotterization. However, constructing a quantum circuit for preparing wave packets is nontrivial, as the particle creation operator is not unitary. Reference [34] addresses this challenge using a quantum circuit inspired by the Jordan-Lee-Preskill protocol [54,55], in which the wave packet preparation is approximated through Trotterization of an auxiliary Hamiltonian. The resulting CNOT gate count scales as $\mathcal{O}(L^3 N_{\mathrm{Trotter}})$ for the general case, where N_{Trotter} denotes the number of Trotter steps. Trotter errors and deep circuits make the accurate state preparation challenging on current noisy devices, which in turn can lead to deviations from the correct results in the subsequent dynamics.

In this section, we present an alternative approach to preparing meson wave packets that avoids these limitations. Our method constructs the desired state exactly, without any Trotter error, and reduces the circuit depth from $\mathcal{O}(L^3)$ to $\mathcal{O}(L)$. The total number of CNOT gates required scales as $\mathcal{O}(L^2)$, and the circuit relies only on nearest- and next-nearest-neighbor connectivity (in fact, only nearest-neighbor connectivity is strictly required, since the next-nearest-neighbor CNOT gates can be compiled into nearest-neighbor ones at a constant factor overhead), making it well suited for current quantum hardware. These improvements in efficiency and accuracy are crucial for scaling to larger system sizes and for ensuring reliable simulation of the dynamics.

More specifically, the initial state we want to prepare consists of the vacuum state $|\Omega\rangle$ and meson creation operators $B^\dagger_{\bar{k},\bar{x}}$ applied to it, as defined in Eq. (20). The vacuum state $|\Omega\rangle$ can be obtained by VQE [31,56] or other techniques [47,57,58]. The operator $B^\dagger_{\bar{k},\bar{x}}$ is nonunitary, making it nontrivial to design a quantum circuit for its implementation. To address this problem, we propose decomposing these operators using Givens rotations [59–61]. For convenience, we define a Hermitian operator $A^\dagger_{\bar{k},\bar{x}} = B^\dagger_{\bar{k},\bar{x}} + B_{\bar{k},\bar{x}}$. In principle, $A^\dagger_{\bar{k},\bar{x}}|\Omega\rangle = B^\dagger_{\bar{k},\bar{x}}|\Omega\rangle$, as $B_{\bar{k},\bar{x}}|\Omega\rangle = 0$ due to the annihilation property $b_k|\Omega\rangle = 0$. Although this equality might be slightly violated when using the operator obtained via QSE, our numerical simulations show that the state $A^\dagger_{\bar{k},\bar{x}}|\Omega\rangle$ achieves a fidelity of 99.9% with the state $B^\dagger_{\bar{k},\bar{x}}|\Omega\rangle$.

The Hermitian operator $A_{\bar{k},\bar{x}}$ can be expressed as

$$A^\dagger_{\bar{k},\bar{x}} = \sum_{nl} \mathcal{M}_{nl}\tilde{\xi}^\dagger_n\tilde{\xi}_l, \tag{25}$$

where $\mathcal{M}_{nl}$ are coefficients corresponding to the wave packet's amplitude ϕ^s_k and the coefficients of vector meson operators $a^{k,-1}_{nl}$, similar as in Eq. (19). The fermionic operators $\tilde{\xi}^\dagger_n$, $\tilde{\xi}_n$ incorporate a string of link variables starting from site 1

$$\tilde{\xi}^\dagger_n = \xi^\dagger_n W_{n,1}, \quad \tilde{\xi}_n = W_{1,n}\xi_n. \tag{26}$$

Thus, the operator $\tilde{\xi}^\dagger_n\tilde{\xi}_l$ is gauge invariant. The coefficient matrix $\mathcal{M}$ is Hermitian and with dimension $L \times L$; hence, it can

be diagonalized as $\mathcal{M} = uDu^\dagger$, where u is a unitary matrix and $D = \mathrm{diag}(\lambda_1, \lambda_2, \ldots, \lambda_L)$ is a real diagonal matrix. This allows us to rewrite the operator $A^\dagger_{\tilde{k},\tilde{x}}$ as

$$\begin{aligned} A^\dagger_{\tilde{k},\tilde{x}} &= \sum_{nlr} \tilde{\xi}^\dagger_n (u_{nr} D_{rr} u^\dagger_{rl}) \tilde{\xi}_l \\ &= \sum_r \left(\sum_n \tilde{\xi}^\dagger_n u_{nr} \right) \lambda_r \left(\sum_l u^*_{lr} \tilde{\xi}_l \right) \\ &= \sum_r (V(u,\tilde{\xi})\, \tilde{\xi}^\dagger_r\, V(u,\tilde{\xi})^\dagger) \lambda_r (V(u,\tilde{\xi})\, \tilde{\xi}_r\, V(u,\tilde{\xi})^\dagger) \\ &= V(u,\tilde{\xi}) O_D V(u,\tilde{\xi})^\dagger, \end{aligned} \tag{27}$$

where $O_D = (\sum_r \lambda_r \tilde{\xi}^\dagger_r \tilde{\xi}_r)$ is diagonal in fermionic Fock basis for the matter sites and the Pauli-Z basis for the links. In the third line, we used the property that a linear combination of fermionic operators can be realized as a unitary transformation.

$$\begin{aligned} \sum_l \tilde{\xi}^\dagger_l u_{ln} &= V(u,\tilde{\xi})\, \tilde{\xi}^\dagger_n\, V(u,\tilde{\xi})^\dagger, \\ \sum_l \tilde{\xi}_l u^*_{ln} &= V(u,\tilde{\xi})\, \tilde{\xi}_n\, V(u,\tilde{\xi})^\dagger, \end{aligned} \tag{28}$$

with $V(u,\tilde{\xi})$ being a unitary operator defined as

$$V(u,\tilde{\xi}) = \exp\left(\sum_{nl} \tilde{\xi}^\dagger_n [\ln u]_{nl} \tilde{\xi}_l \right). \tag{29}$$

The proof of Eq. (28) is provided in Appendix C. In the following, we will introduce the quantum circuit corresponding to Eq. (27). Specifically, we will introduce the circuit for $V(u,\tilde{\xi})$ in Sec. V A, where we will closely follow the methods introduced in Ref. [26]. The implementation of the diagonal part O_D is discussed in Sec. V B, before we provide a resource estimation for the full circuit implementing the operator $A^\dagger_{\tilde{k},\tilde{x}}$ in Sec. V C.

A. Circuit for $V(u,\tilde{\xi})$

The operator $V(u,\tilde{\xi})$ mathematically has the same structure as the one in Ref. [26], although the model considered here is not a purely fermionic one, in contrast to the reference. Hence, we can closely follow the methods developed therein to find a circuit implementing it. In particular, $V(u,\tilde{\xi})$ satisfies the homomorphism property under matrix multiplication, i.e., $V(v,\tilde{\xi}) \times V(u,\tilde{\xi}) = V(v \times u, \tilde{\xi})$, which is proven in Appendix C. Utilizing this property, $V(u,\tilde{\xi})$ can be decomposed into local operators with a QR decomposition of u via Givens rotations, as shown in Refs. [60,61]. In summary, $V(u,\tilde{\xi})$ can be decomposed by $L(L-1)/2$ local operators with $2L-3$ layers [60]. Specifically, the local operators corresponding to the Givens rotations are of the following form:

$$\begin{aligned} R^\dagger_{nl}(\theta,\tilde{\xi}) &= \exp(\theta_{n,l}[\tilde{\xi}^\dagger_{n-1}\tilde{\xi}_n - \tilde{\xi}^\dagger_n \tilde{\xi}_{n-1}]) \\ &= \exp(\theta_{n,l}[\xi^\dagger_{n-1} Z_{g,n-1} \xi_n - \xi^\dagger_n Z_{g,n-1} \xi_{n-1}]) \\ &\overset{\text{JWT}}{=} \exp\left(-i \frac{\theta_{n,l}}{2} \left[\sigma^x_{n-1} Z_{g,n-1} \sigma^x_n + \sigma^y_{n-1} Z_{g,n-1} \sigma^y_n \right] \right), \end{aligned} \tag{30}$$

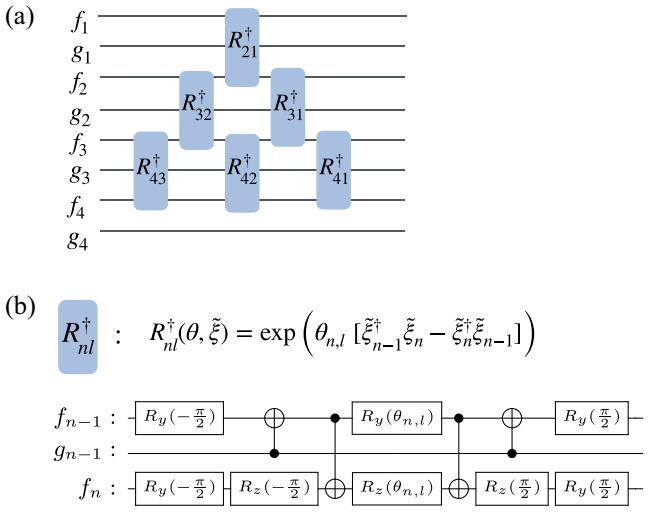

FIG. 7. (a) Decomposition of $V(u,\tilde{\xi})$ for a system with $L = 4$ using six Givens rotations. (b) Decomposition of the local Givens rotations $R^\dagger_{nl}(\theta,\tilde{\xi})$ into four CNOT gates and single-qubit rotation gates. Qubits labeled as f_n represent the matter field at site n, and the qubits labeled as g_{n-1} represent the gauge field on the link between the sites $n-1$ and n.

where $\theta_{n,l}$ is determined by the ratio of matrix elements in u, as detailed in Appendix A of Ref. [26]. These operators are a specific instance of the general construction in Eq. (29), chosen to eliminate the matrix element u_{nl} via Givens rotation [62]. For clarity, we omit the single-qubit rotation gates associated with the complex phases of the matrix elements, which are also described in Appendix A of Ref. [26]. The final expression in Eq. (30) follows from applying the Jordan-Wigner transformation in Eq. (4).

To illustrate the result, we take an example with four sites and show the circuit for $V(u,\tilde{\xi})$ in Fig. 7(a). The decomposition of $R^\dagger_{nl}(\theta,\tilde{\xi})$ in standard single and two-qubit gates is depicted in Fig. 7(b) and comprises four CNOT gates. In total, the decomposition of $V(u,\tilde{\xi})$ for a system with L sites requires $2L(L-1)$ CNOT gates and results in a circuit depth of $8L-12$.

B. Circuit for the diagonal operator O_D

The diagonal part O_D in Eq. (27) also needs to be decomposed into quantum gates. This operator is not present in earlier constructions, and here we provide a circuit implementation using an ancilla qubit whose depth is linear in system size. After applying the JWT, the diagonal part reads

$$O_D = \frac{I}{2} \sum_n \lambda_n + \frac{\lambda_1}{2}\sigma^z_1 + \frac{\lambda_2}{2}\sigma^z_2 + \cdots + \frac{\lambda_L}{2}\sigma^z_L. \tag{31}$$

To find a circuit implementing O_D, we consider a more general expression, which includes the above equation as a special case

$$O_D = \sum_{n<L} \lambda_n P_n, \tag{32}$$

with $P_n \in \{I, \sigma^x, \sigma^y, \sigma^z\}^{\otimes L}$ a Pauli string and we require $[P_n, P_l] = 0$. To realize such a linear combination of Pauli

operators, we need to define some ancillary fermionic operators on the qubits representing the gauge field, which will ultimately have no effect on these qubits. To distinguish these from the fermionic operators ξ representing the matter fields, we define these ancillary fermionic operators as

$$\begin{aligned}\psi^\dagger_{g,n} &= \prod_{l<n}(-iZ_{g,l})\frac{X_{g,n}+iY_{g,n}}{2},\\ \psi_{g,n} &= \prod_{l<n}(iZ_{g,l})\frac{X_{g,n}-iY_{g,n}}{2},\\ \tilde{X}_{g,n} &= \frac{\psi^\dagger_{g,n}+\psi_{g,n}}{\sqrt{2}},\end{aligned} \tag{33}$$

where the operators $X_{g,n}, Y_{g,n}, Z_{g,n}$ are Pauli operators acting on the gauge field qubits as before. The operators defined in Eq. (33) fulfill the anticommutation relations

$$\begin{aligned}\{\psi^\dagger_{g,n}, \psi_{g,l}\} &= \delta_{n,l},\\ \{\psi_{g,n}, \psi_{g,l}\} &= \{\psi^\dagger_{g,n}, \psi^\dagger_{g,l}\} = 0,\\ \{\tilde{X}_{g,n}, \tilde{X}_{g,l}\} &= \delta_{n,l}.\end{aligned} \tag{34}$$

In addition, all of them commute with Pauli strings P_n acting on the matter sites, as they operate on disjoint sets of qubits.

Using these, we can consider another set of operators given by

$$O_a = \sum_n \mathrm{sgn}(\lambda_n)\sqrt{|\lambda_n|}\tilde{X}_{g,n}, \quad O_b = \sum_n \sqrt{|\lambda_n|}P_n\tilde{X}_{g,n}, \tag{35}$$

with real values λ_n. This is motivated by the fact that the values λ_n in Eq. (27) correspond to eigenvalues of the Hermitian matrix $\mathcal{M}$. In the expression above, $\mathrm{sgn}(\lambda_n)$ represents the sign of λ_n. These operators satisfy the identity

$$\{O_a, O_b\} = \sum_n \lambda_n P_n. \tag{36}$$

The above equation utilizes the property of Eq. (34) and the final result is exactly O_D in Eq. (32) as desired. Hence, the problem of realizing O_D reduces to decomposing the operators O_a and O_b into a quantum circuit. Once these circuits are constructed, the above anticommutator can be realized using a Hadamard test. O_a can be expressed as a linear combination of fermion operators and can be decomposed by Givens rotation, similar to Eq. (28):

$$\begin{aligned}O_a &= \sum_n \mathrm{sgn}(\lambda_n)\sqrt{|\lambda_n|}\tilde{X}_{g,n}\\ &= \sum_n \mathrm{sgn}(\lambda_n)\sqrt{\frac{\lambda_n}{2}}(\psi^\dagger_{g,n}+\psi_{g,n})\\ &= V(u_a,\psi_g)(\psi^\dagger_{g,1}+\psi_{g,1})V(u_a,\psi_g)^\dagger\\ &= V(u_a,\psi_g)X_{g,1}V(u_a,\psi_g)^\dagger,\end{aligned} \tag{37}$$

where the first column of the matrix u_a relates the coefficients in O_a, i.e., $1/\sqrt{2\mathcal{N}_\lambda}\times(\mathrm{sgn}(\lambda_1)\sqrt{|\lambda_1|}, \mathrm{sgn}(\lambda_2)\sqrt{|\lambda_2|}, \ldots)^T$, with $\mathcal{N}_\lambda$ being a normalization factor [63]. Since we are only concerned with the first column of u_a, $V(u_a,\psi_g)$ can be decomposed with $L-1$ Givens rotations, consists of local operators as in Eq. (30), but with operator ψ_g in the formula,

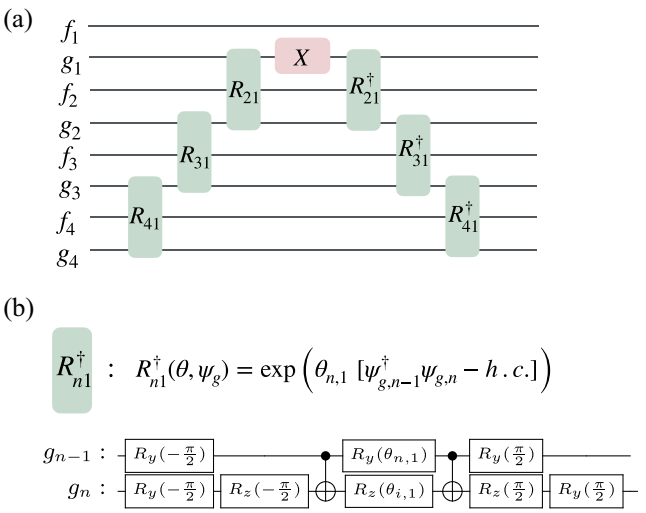

FIG. 8. (a) Illustration of the circuit for O_a for $L=4$. The first three Givens rotation gates correspond to the decomposition of $V(u_a,\psi_g)^\dagger$ and the last three are for $V(u_a,\psi_g)$. Again, the phase gates are not shown for simplicity. (b) Decomposition of a local Givens rotation gate $R^\dagger_{n1}(\theta,\psi_g)$, which performs the rotation between two nearest-neighbor qubits representing the gauge fields, and can be implemented with standard gates using two CNOT operations.

i.e., $R^\dagger_{n,1}(\theta,\psi_g)$. We show the circuit for O_a in Fig. 8(a), which consists of $2(L-1)$ Givens rotations and can be decomposed into a total of $4(L-1)$ CNOT gates. Notice that dynamical decoupling techniques [64,65] can efficiently suppress error accumulation caused by long idle times. Such techniques are routinely implemented on current quantum hardware.

Regarding O_b, similar to the case of $\tilde{\xi}$, we can define the fermionic operator $\tilde{\psi}_{g,n} = P_n\psi_{g,n}$. Since $P_n^2 = I$, and $\tilde{\psi}_{g,n}, \tilde{\psi}^\dagger_{g,n}$ still satisfy the standard fermionic anticommutation relations

$$\begin{aligned}\{\tilde{\psi}_{g,n}, \tilde{\psi}^\dagger_{g,l}\} &= P_nP_l\{\psi_{g,n}, \psi^\dagger_{g,l}\} = \delta_{n,l},\\ \{\tilde{\psi}_{g,n}, \tilde{\psi}_{g,l}\} &= P_nP_l\{\psi_{g,n}, \psi_{g,l}\} = 0,\end{aligned} \tag{38}$$

O_b can be written as

$$\begin{aligned}O_b &= \sum_n \sqrt{|\lambda_n|}P_n\tilde{X}_{g,n}\\ &= V(u_b,\tilde{\psi}_g)(\tilde{\psi}^\dagger_{g,1}+\tilde{\psi}_{g,1})V(u_b,\tilde{\psi}_g)^\dagger\\ &= V(u_b,\tilde{\psi}_g)X_{g,1}V(u_b,\tilde{\psi}_g)^\dagger.\end{aligned} \tag{39}$$

Here, the first column of u_b is $1/\sqrt{2\mathcal{N}_\lambda}\times(\sqrt{|\lambda_1|}, \sqrt{|\lambda_2|}, \ldots)^T$, and $P_1 = I$. Similar to $V(u_a,\psi)$, $V(u_b,\tilde{\psi})$ can be decomposed into $L-1$ Givens rotations, where each of these is implemented by a circuit like the one shown in Fig. 8(a), but with the Givens rotation gates being $R^\dagger_{n,1}(\theta,\tilde{\psi})$:

$$\begin{aligned}R^\dagger_{n,1}(\theta,\tilde{\psi}) &= \exp(\theta_{n,1}[\tilde{\psi}^\dagger_{n-1}\tilde{\psi}_n - \tilde{\psi}^\dagger_n\tilde{\psi}_{n-1}])\\ &= \exp\left(-i\frac{\theta_{n,1}}{2}P_{n-1}P_n[X_{g,n-1}X_{g,n} + Y_{g,n-1}Y_{g,n}]\right)\end{aligned} \tag{40}$$

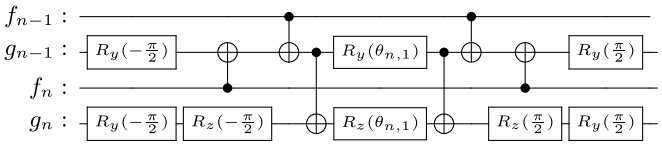

FIG. 9. Circuit of $R^{\dagger}_{n,1}(\theta, \tilde{\psi})$ for decomposing O_b, with operator $P_1 = I$, $P_n = \sigma^z_{n-1}$ for $n > 1$ in Eq. (35).

These can be implemented with six CNOT gates as shown in Fig. 9. All in all, O_b can be implemented with $2(L-1)$ Givens rotation gates, and $12(L-1)$ CNOT gates.

C. Full circuit for wave packet preparation

Finally, we present the complete circuit for preparing a meson wave packet in Fig. 10. Additionally, we summarize the number of CNOT gates and the circuit depths in Table I, assuming both nearest-neighbor and next-nearest-neighbor connectivity. For simplicity, we do not include the constant factor overhead of compiling next-nearest-neighbor CNOT gates into nearest-neighbor ones, which would be required on hardware with only nearest-neighbor connectivity. It is worth noting that the estimation does not account for potential parallelization between different parts of the circuit, which could slightly reduce the circuit depth. Moreover, the depth could be further reduced with higher connectivity, which allows greater parallelization of Givens rotation. The anticommutator $\{O_a, O_b\}$ is implemented by the Hadamard test, where the control gate on O_a only requires a controlled-X gate, because the rest of the operator is identity if we remove the X gate, as shown in Fig. 8(a). Therefore, there are only two extra CNOT gates introduced by the Hadamard test; we will ignore them in the overall resource estimation for simplicity.

Note that for large systems and narrow wave packets, where $L \gg 1/\sigma_k$, only the qubits involved in the region in which the wave packet is nontrivial need to be considered in the circuit for preparing the wave packet. In such cases, the parameter L in Table I can be effectively replaced by $\Lambda \sim 1/\sigma_k$.

TABLE I. Resource estimation for preparing a meson wave packet. The total two-qubit gate count and circuit depth include one $V(u, \tilde{\xi})$ and one $V(u, \tilde{\xi})^{\dagger}$, two O_a, and one O_b, as illustrated in Fig. 10. For a narrow wave packet, L can be replaced with $\Lambda \sim 1/\sigma_k$.

	CNOT gates	CNOT depth
$V(u, \tilde{\xi})$ or $V(u, \tilde{\xi})^{\dagger}$	$2L(L-1)$	$4(2L-3)$
O_a	$4(L-1)$	$4(L-1)$
O_b	$12(L-1)$	$12(L-1)$
Total	$4L^2 + 16L - 20$	$36L - 44$

VI. SUMMARY AND OUTLOOK

In this work, we develop a scalable and general framework for preparing meson wave packets with well-defined momentum and charge conjugation quantum numbers in a $\mathbb{Z}_2$ LGT. Using a symmetry-preserving QSE approach, we constructed high-fidelity meson creation operators across a wide range of parameters. Importantly, the QSE requires only the expected values of operators in the ground state, making it broadly applicable both to quantum platforms and to classical Hamiltonian simulation methods such as TN methods. These operators, superimposed with a spatially localized Gaussian profile, allow for the construction of spatially separated wave packets that serve as the initial state of the scattering experiment. The method avoids variational optimization of parametrized quantum circuits, is systematically improvable, and offers the flexibility to choose between quantum or classical implementations for optimal efficiency.

Utilizing this technique, we can prepare two spatially separated meson wave packets with opposite momenta and simulate their real-time scattering dynamics using MPS. We observe both elastic and inelastic scattering processes across a range of model parameters and characterize the process in terms of local observables such as the site-resolved fermion and electric field density, as well as studying the energy transfer, meson number, and the probability of observing a single flux string. These observables allow us to get a comprehensive insight into the scattering process. In particular, we observe the formation of strings during the collision followed by string breaking and hadronization. In the case of inelastic scattering, this process is accompanied by a significant increase in the electric energy contribution and a decrease in the kinetic energy, indicating the formation of particles, which also show a clear signal in the meson number. Our results thus provide a comprehensive characterization of particle collisions and insight into the dynamics of inelastic scattering processes, inaccessible with conventional lattice methods.

In addition, for the inelastic case we observe a significant growth in the bipartite entanglement entropy, which saturates at high values after the collision, thus motivating the implementation on quantum devices. To this end, we develop an efficient and accurate quantum circuit for meson wave packet preparation based on Givens rotations. For a system with L sites, this decomposition yields a circuit with depth $\mathcal{O}(L)$ and requires $\mathcal{O}(L^2)$ CNOT gates, making it well suited for implementations on near-term quantum devices.

In this work, we used a $\mathbb{Z}_2$ gauge theory as a representative example. The approach for generating meson wave packets is not limited to this setting and can be readily extended to other gauge models, such as the Schwinger model, and to higher-dimensional LGTs. Hence, it provides a stepping stone

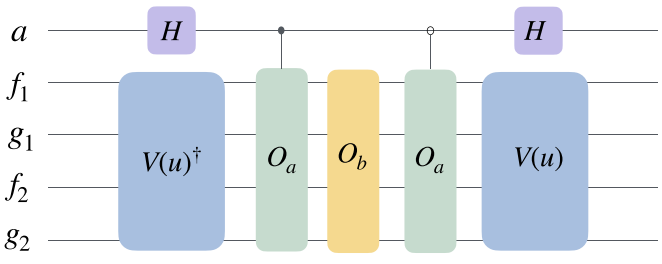

FIG. 10. Sketch of the full circuit for preparing a meson wave packet. The qubit labeled a is an ancilla qubit required for the Hadamard test. The individual operators $V(u)$, O_a, and O_b can be decomposed in standard single and two-qubit gates as outlined in the text.

toward studying real-time dynamics of scattering processes in more complicated gauge theories and for a characterization of complex phenomena, such as hadronization and fragmentation, beyond the capabilities of conventional lattice methods.

Note added. Two related publications appeared concurrently with our work. Reference [66] reports a quantum experiment of hadron scattering in a quantum link model using IBM's `ibm_marrakesh` quantum computer. Reference [67] presents a meson scattering experiment in the same $\mathbb{Z}_2$ LGT as considered here, performed on the trapped-ion platform `IonQ Forte`, with a focus on improving VQE-based meson operator construction and demonstrating early-time dynamics. In contrast, our work develops a scalable framework for preparing particle wave packets using a non-variational quantum subspace expansion method, along with an accurate circuit decomposition based on Givens rotations. We further explore the full scattering process, including inelastic dynamics and hadronization. Together with Ref. [67], our study represents a complementary effort, addressing both algorithmic and experimental aspects of quantum simulations of scattering.

ACKNOWLEDGMENTS

The authors thank Lingxiao Xu and Karl Jansen for very helpful discussions. Y.C. thanks Liuming Liu and Peng Sun for constructive discussions on lattice QCD. This work was supported with funds from the Ministry of Science, Research and Culture of the State of Brandenburg within the Center for Quantum Technology and Applications (CQTA).

DATA AVAILABILITY

There are no publicly available research data or software supporting this manuscript. Requests for further information or data should be sent to the authors.

APPENDIX A: QUANTUM SUBSPACE EXPANSION

In this Appendix, we provide details on the QSE method used in our work. Reference [68] offers a concise review of QSE in Appendix S1. Here, we extend the approach to include the additional constraints in our setup, namely, the conditions that mesons should be an eigenstate of the charge conjugation operator C and be annihilated by the operator $b_{k,c}$. As introduced in Ref. [68], a commonly employed strategy for obtaining the eigenstates of a Hamiltonian is based on the Ritz variational principle [69]. This approach involves minimizing the following cost function for the quantum state $|\tilde{\psi}\rangle = \sum_I a_I M_I|\Omega\rangle$, defined within the subspace specified in Eq. (14),

$$\begin{aligned}\mathcal{L} &= \langle\tilde{\psi}|H|\tilde{\psi}\rangle - \lambda(\langle\tilde{\psi}|\tilde{\psi}\rangle - 1)\\ &= \sum_{I,J} a_I^* a_J \,\langle\Omega|M_I^\dagger H M_J|\Omega\rangle\\ &\quad - \lambda\left(\sum_{I,J} a_I^* a_J \,\langle\Omega|M_I^\dagger M_J|\Omega\rangle - 1\right),\end{aligned} \tag{A1}$$

where the λ is the Lagrange multiplier to enforce the normalization of the wave function. From the stationarity condition, $\partial_{a_I^*}\mathcal{L} = 0$, the following generalized eigenvalue equation can be derived

$$\mathcal{H}\vec{a} = \lambda\mathcal{S}\vec{a}, \tag{A2}$$

where $\mathcal{H}$ and $\mathcal{S}$ are matrix elements as in Eq. (15). By solving the above equation, we can obtain the coefficients $\vec{a} = (a_{1,1}, a_{1,2}, \ldots, a_{2,1}, a_{2,2}, \ldots)$ that yield the eigenstate, with λ being an eigenvalue E of the Hamiltonian.

In this work, we also want to impose that the solution is an eigenstate of the operator C, which commutes with Hamiltonian; hence, there exists a common set of eigenfunctions. Besides, the annihilation condition, $b_{k,c}|\Omega\rangle = 0$, needs to be included, too. The corresponding generalization of Eq. (A1) then reads as

$$\begin{aligned}\mathcal{L} &= \langle\Omega|b_{k,c}\, H\, b_{k,c}^\dagger|\Omega\rangle + \langle\Omega|b_{k,c}\, C\, b_{k,c}^\dagger|\Omega\rangle + \langle\Omega|b_{k,c}^\dagger b_{k,c}|\Omega\rangle\\ &\quad - \lambda(\langle\Omega|b_{k,c}b_{k,c}^\dagger|\Omega\rangle - 1)\\ &= \sum_{I,J} a_I^{(k,c)*}\, a_J^{(k,c)}\,\langle\Omega|M_I^\dagger H M_J|\Omega\rangle\\ &\quad + \sum_{I,J} a_I^{(k,c)*}\, a_J^{(k,c)}\,\langle\Omega|M_I^\dagger C M_J|\Omega\rangle\\ &\quad + \sum_{I,J} a_I^{(k,c)*}\, a_J^{(k,c)}\,\langle\Omega|M_J M_I^\dagger|\Omega\rangle\\ &\quad - \lambda\left(\sum_{I,J} a_I^{(k,c)*}\, a_J^{(k,c)}\,\langle\Omega|M_I^\dagger M_J|\Omega\rangle - 1\right).\end{aligned} \tag{A3}$$

Here, we label the coefficients with superscripts since the solution will also yield an eigenstate of C with eigenvalue c and momentum k. By imposing $\partial_{a_I^{k,c*}}\mathcal{L} = 0$, we can obtain the following equation:

$$(\mathcal{H} + \mathcal{C} + \mathcal{Z})\,\vec{a}^{(k,c)} = \lambda\,\mathcal{S}\vec{a}^{(k,c)}, \tag{A4}$$

where the matrices $\mathcal{C}$, $\mathcal{Z}$ are the same as Eq. (16). The values λ now include various contributions: $\lambda = E + ce^{-ika} + \langle\Omega|b_{k,c}^\dagger b_{k,c}|\Omega\rangle$. Ideally, the last term should vanish; however, due to the finite basis employed, it generally yields nonzero, albeit small, values.

APPENDIX B: PERFORMANCE OF QSE

To enable a direct comparison with Ref. [34], we present a heat map of the infidelity across a grid of (m, ε) values at fixed system size $L = 30$. For each parameter point, we compute the ground state and the first ten excited states using both direct MPS simulation and our QSE approach, and then evaluate the fidelity F between the corresponding states. The infidelity in a logarithmic scale $\log_{10}(1 - F)$ is shown in Fig. 11. The color scale is chosen to match Fig. 5 of Ref. [34] for easier visual comparison. We present three representative momenta of vector mesons in the figure. The result indicates small ε values at $m \sim 0.1$ present greater challenges, particularly at low momentum. Nonetheless, the fidelity remains above 0.99 throughout the parameter space, including for higher momenta.

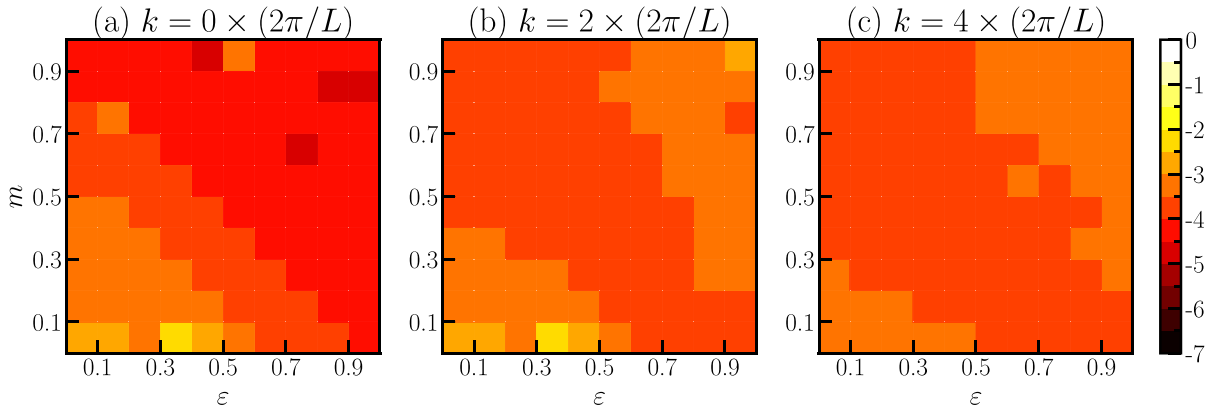

FIG. 11. Heat map of the infidelities presented on a logarithmic scale, $\log_{10}(1 - F)$, as indicated by the color bar in the (m, ε) plane for $L = 30$. The different panels correspond to distinct momentum values: (a) $k = 0$, (b) $k = 2 \times (2\pi/L)$, and (c) $k = 4 \times (2\pi/L)$.

To further assess scalability, we study how the fidelity behaves as the system size increases. For system sizes from $L = 30$ to $L = 60$, we compute the lowest ten excited states using both QSE and MPS at fixed parameters $(m, \varepsilon) = (0.3, 0.3)$ and evaluate the fidelity between them. To reduce simulation cost, we restrict the operator pool to fermion-antifermion operators with Wilson-line length shorter than 10, which is motivated by confinement as indicated in Fig. 3 in the main text. For the regime we consider, all of states correspond to different momentum excitations of the vector meson. We focused on two representative low-energy excitations and benchmarked their fidelities across system sizes.

As shown in Fig. 12(a), both momenta maintain fidelities above 0.999 even at $L = 60$ (120 qubits). There is a very mild, gradual decrease in fidelity as system size increases. It is worth noting that the fidelity is computed relative to MPS states, which are themselves approximations, and when computing excited states, errors can accumulate. The algorithm for excitations is based on modifying the Hamiltonian by adding a sufficiently large energy penalty term to push up the previously calculated low-energy states, and the energy gradually grows with system size; this also leads to the larger errors for highly excited states.

To estimate how close the QSE-prepared states are to exact eigenstates, we analyze the fluctuations of conserved quantities, specifically the energy and the charge conjugation operator. These should vanish for an exact eigenstate:

$$\Delta O = \sqrt{|\langle O^2\rangle - \langle O\rangle^2|}, \quad O \in \{H, C\}. \tag{B1}$$

In Fig. 12(b), the MPS ground state exhibits small energy fluctuations, while its excited states show increasing fluctuations with system size, likely due to loss of translational symmetry and accumulated truncation errors. In contrast, the excited states extracted with QSE show slightly decreasing energy fluctuations as the system grows, comparable to the behavior of the vacuum.

Moreover, Fig. 12(c) shows the fluctuations of the charge conjugation operator. Here, QSE shows signs of advantage over simulation by MPS with OBC: The QSE states preserve the charge conjugation quantum number much more faithfully across system sizes. This is expected, as MPS states do not conserve translation symmetry by construction, and the charge conjugation operator in staggered fermions mixes with translation [see Eqs. (3) and (12)]. In contrast, QSE explicitly restores both translation and charge conjugation symmetry by diagonalizing the operator C in subspace, ensuring ΔC remains minimal, even for higher excited states.

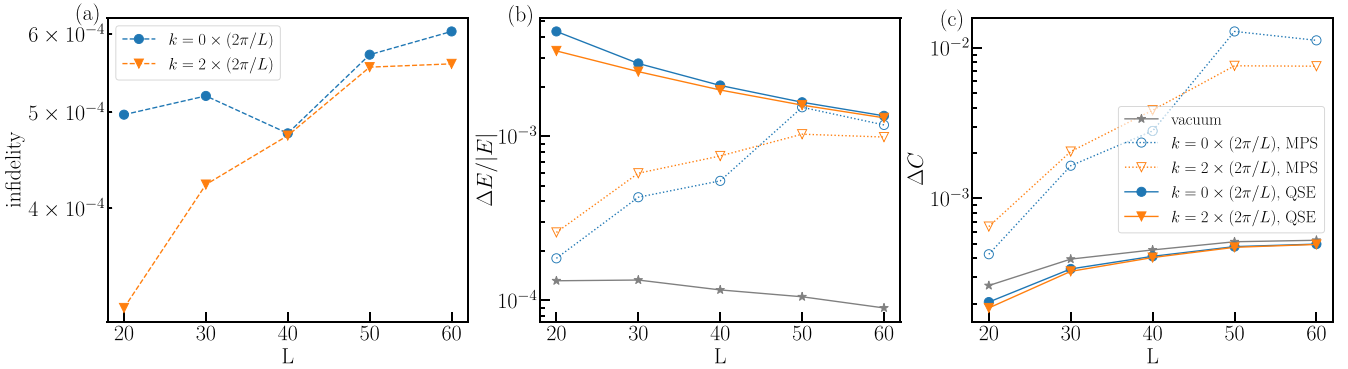

FIG. 12. Performance scaling of QSE with system size up to 60 sites (120 qubits), for fixed parameters $(m, \varepsilon) = (0.3, 0.3)$. Two momentum modes are shown: $k = 0 \times (2\pi/L)$ (blue dots) and $k = 2 \times (2\pi/L)$ (orange triangles). (a) Infidelity between QSE and direct MPS results. (b) Relative energy fluctuation of the QSE states (solid markers with lines) and MPS states (empty markers with dashed lines). The vacuum obtained from MPS simulation is also shown as a reference (gray star). (c) Charge conjugation fluctuation of the QSE states and MPS states.

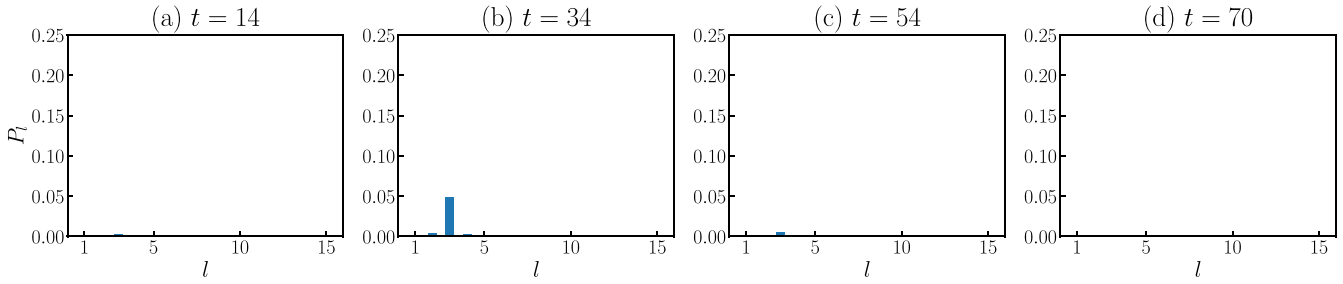

FIG. 13. P_l at different times with $m = 0.1, \varepsilon = 1.0, \bar{k} = 6 \times (2\pi)/L$, corresponding to the elastic scattering process shown in Fig. 4. (a) Time slice before collision, where the two meson wave packets start to overlap, and the two separate flux strings associated with each meson start to merge into a longer single string. (b) Time slice during the collision, the overlap between two wave packets is enhanced and single flux tube is generated. (c) Shortly after the collision, the single flux string breaks and corresponding probability decreases. (d) The time when two mesons are well separated, where the probability for a single flux string remaining is essentially zero, indicating that the strings broke and hadronized into the outgoing mesons.

APPENDIX C: GIVENS ROTATION FOR FERMIONIC OPERATORS

References [60,61] have already demonstrated that the unitary transformation of the single-particle basis for fermions can be realized using Givens rotations. Here, we extend this idea from fermions to general fermionic operators, showing that Givens rotation can be applied to arbitrary operators, e.g., to fermion operators coupled with bosonic operators, as long as the anticommutation relations hold. Specifically, this applies to the operators $\tilde{\xi}_n$ defined in Eq. (26). The proof of Eq. (28) follows a similar approach to the Appendix of Ref. [60]. For completeness, we present the proof below.

For the fermionic operators $\tilde{\xi}_n^\dagger, \tilde{\xi}_n$, the usual anticommutation relations are satisfied

$$\{\tilde{\xi}_n^\dagger, \tilde{\xi}_l\} = \delta_{nl}, \quad \{\tilde{\xi}_n, \tilde{\xi}_l\} = \{\tilde{\xi}_n^\dagger, \tilde{\xi}_l^\dagger\} = 0. \tag{C1}$$

Hence, for the operator $K = \sum_{nl} \ln(u)_{nl} \tilde{\xi}_n^\dagger \tilde{\xi}_l$, with u being a unitary matrix, the following equations hold

$$[K, \tilde{\xi}_r^\dagger] = \sum_n \tilde{\xi}_n^\dagger \ln(u)_{nr}, \quad [K, \tilde{\xi}_r] = \sum_n \tilde{\xi}_n \ln(u)^*_{nr}. \tag{C2}$$

Considering the transformation by operator $V(u, \tilde{\xi}) = e^K$, one finds

$$\begin{aligned} V(u, \tilde{\xi}) \tilde{\xi}_r^\dagger V(u, \tilde{\xi})^\dagger &= e^K \tilde{\xi}_r^\dagger e^{-K} && \text{(C3)} \\ &= \tilde{\xi}_r^\dagger + [K, \tilde{\xi}_r^\dagger] + \frac{1}{2}[K, [K, \tilde{\xi}_r^\dagger]] \cdots && \text{(C4)} \\ &= \tilde{\xi}_r^\dagger + \sum_n \tilde{\xi}_n^\dagger \ln(u)_{nr} \\ &\quad + \frac{1}{2} \sum_{nl} \tilde{\xi}_l^\dagger \ln(u)_{ln} \ln(u)_{nr} \cdots && \text{(C5)} \\ &= \sum_n \tilde{\xi}_n^\dagger \left\{ \delta_{nr} + \ln(u)_{nr} + \frac{1}{2} \ln(u)^2_{nr} \cdots \right\} && \text{(C6)} \\ &= \sum_n \tilde{\xi}_n^\dagger u_{nr}, && \text{(C7)} \end{aligned}$$

where we used the Baker-Campbell-Hausdorff expansion in the second line.

Next, we show that $V(u, \tilde{\xi})$ satisfies the homomorphism property under matrix multiplication. With two unitary matrices u and v, $V(v, \tilde{\xi}) \times V(u, \tilde{\xi}) = V(v \times u, \tilde{\xi})$, which can be proven as follows:

$$\begin{aligned} &V(v, \tilde{\xi}) V(u, \tilde{\xi}) \tilde{\xi}_r^\dagger V(u, \tilde{\xi})^\dagger V(v, \tilde{\xi})^\dagger \\ &= V(v, \tilde{\xi}) \left(\sum_n \tilde{\xi}_n^\dagger u_{nr} \right) V(v, \tilde{\xi}) \\ &= \sum_{nl} \tilde{\xi}_l^\dagger v_{ln} u_{nr} \\ &= \sum_l \tilde{\xi}_l^\dagger (vu)_{lr} \\ &= V(vu, \tilde{\xi}) \tilde{\xi}_r^\dagger V(vu, \tilde{\xi})^\dagger. \end{aligned} \tag{C8}$$

The above equation holds for arbitrary $\tilde{\xi}_r^\dagger$, so we conclude $V(v, \tilde{\xi}) \times V(u, \tilde{\xi}) = V(v \times u, \tilde{\xi})$.

APPENDIX D: SINGLE FLUX TUBE GENERATION AND STRING BREAKING

In Figs. 13–17, we present the probabilities P_l for having a single flux tube of length l during the scattering dynamics. To characterize the string generation and breaking, we select four representative time slices for all cases: one before the collision, one during the collision, one shortly after the collision, and a final one where the mesons have propagated for some time after the collision. The initial value of P_l at $t = 0$ is zero for all cases, because the initial state consists of two separate flux strings. Hence, the probability of finding a single flux tube is zero; thus, we do not show these plots.

APPENDIX E: MPS SIMULATION DETAILS

In this work, we use MPS for our classical numerical simulations. For a system with open boundary conditions and N sites, the ansatz is given by [70–72]

$$|\psi\rangle = \sum_{i_1, i_2, \cdots, i_N}^{d} A_1^{i_1} A_2^{i_2} \cdots A_N^{i_N} |i_1\rangle \otimes |i_2\rangle \otimes \cdots \otimes |i_N\rangle, \tag{E1}$$

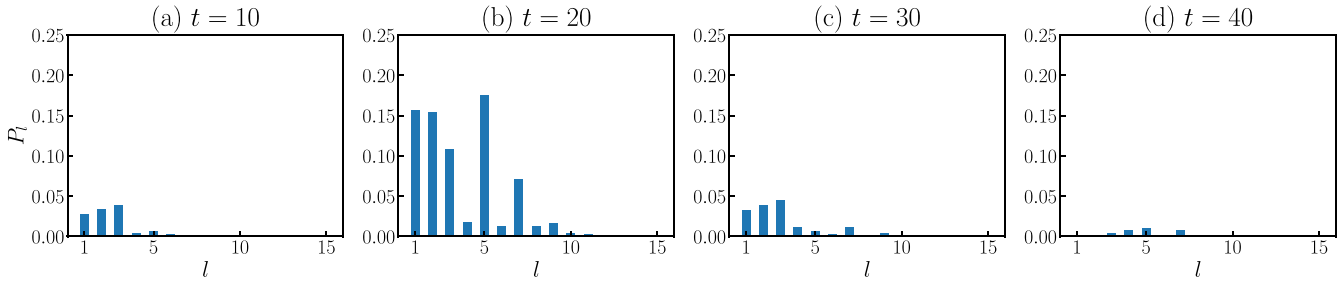

FIG. 14. P_l at different times with $m = 0.1$, $\varepsilon = 0.2$, $\bar{k} = 4 \times (2\pi)/L$, corresponding to the inelastic scattering process shown in the first column of Fig. 5. Compared to the elastic case, more and longer single flux strings are generated due to the smaller electric field energy. (a) Before the collision, the two mesons approach and longer strings begin to form. (b) During the collision, fermion-antifermion annihilation is enhanced as shown in Fig. 5(a), leading to significant generation of strings. (c) Shortly after the collision, the single flux string breaks and the corresponding probabilities decrease. (d) When the two mesons are well separated, most strings are broken, indicating hadronization again into outgoing mesons.

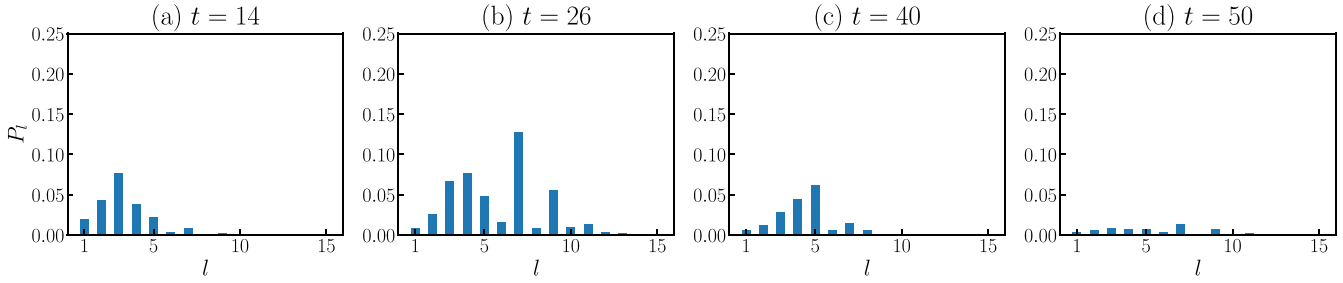

FIG. 15. P_l at different times with $m = 0.1$, $\varepsilon = 0.2$, $\bar{k} = 6 \times (2\pi)/L$, corresponding to the inelastic scattering process shown in the second column of Fig. 5. (a) Time slice before the collision. (b) During the collision, there is an enhanced probability for forming longer strings with $l = 10$ compared to Fig. 14, due to the higher momentum in this case. (c) Shortly after the collision, the probabilities for having a long flux tube decrease again. (d) When the two mesons are well separated, we observe similar situation as for the smaller momentum.

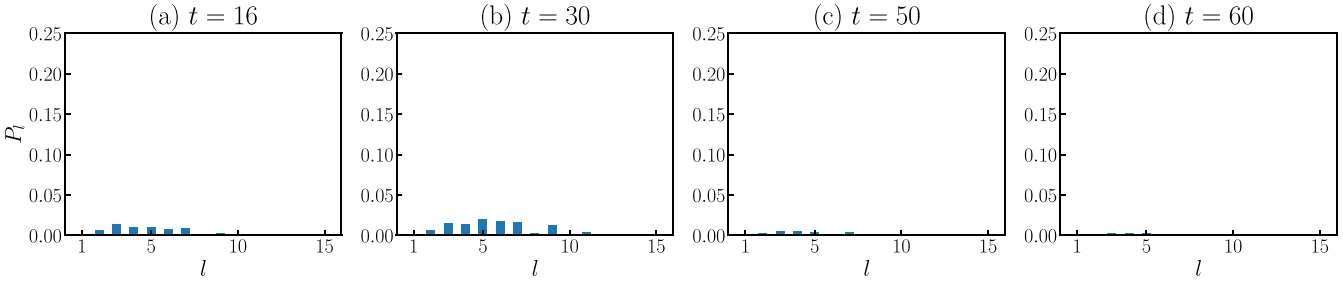

FIG. 16. P_l at different times for $m = 0.1$, $\varepsilon = 0.2$, and $\bar{k} = 8 \times (2\pi/L)$, corresponding to the inelastic scattering process shown in the third column of Fig. 5. Compared to the previous two inelastic scattering cases with lower momentum, a smaller probability of forming a single flux string is observed here, indicating a faster hadronization process. (a) Before the collision. (b) During the collision. (c) Shortly after the collision. (d) After the collision when the two mesons are well separated again.

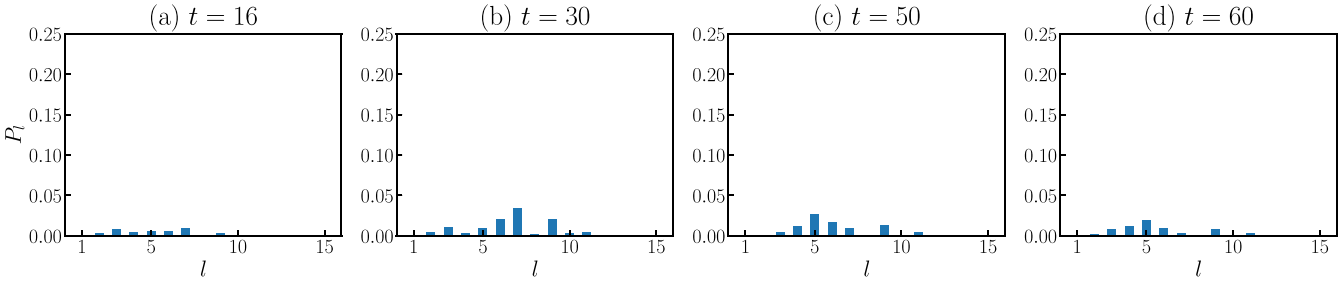

FIG. 17. P_l at different times for $m = 0.2$, $\varepsilon = 0.2$, and $\bar{k} = 8 \times (2\pi/L)$, corresponding to the inelastic scattering process shown in the fourth column of Fig. 5. (a) Before the collision. (b) During the collision. (c) Shortly after the collision. (d) After the collision when the two mesons are well separated.

where d is the local dimension of the Hilbert space on every site and $|i_k\rangle_{k=1}^{d}$ is a local basis for the Hilbert space at site k. The quantities $A_k^{i_k}$ are complex $D \times D$ matrices for $1 < k < N$ and $A_1^{i_1}$ ($A_N^{i_N}$) is a complex D-dimensional row (column) vector. The parameter D, which determines the number of parameters in the ansatz, is called the bond dimension of the MPS and limits the maximum von Neumann entropy in the state, $S \leqslant \log_2 D$, which is in turn a measure for the amount of quantum correlations. For our numerical simulations, we use the ITensor library [52]. Note that while we are using periodic boundary conditions for our Hamiltonian, we nevertheless use MPS with open boundary conditions. This introduces long-range terms, which connect the first and the last site in the MPS, and can potentially lead to long-range correlations requiring a larger value of D to be captured. This decision is motivated by the fact that MPS algorithms using open boundary are in general more efficient and stable than their counterparts for periodic boundary conditions [70].

More specifically, for computing ground states and excitations, we use standard variational methods and optimize the tensors iteratively such that the energy expectation value is minimized. For constructing the basis required for the QSE and the simulation of time evolution, we use TEBD, where we apply local operators to the MPS and reduce the bond dimension of the resulting state by performing a singular value decomposition and discarding all singular values that are smaller than a given threshold, also referred to as cutoff. For the QSE used to construct meson creation operators and to generate eigenstates, we use a cutoff of 10^{-10}. When simulating the scattering dynamics, we set the cutoff to 10^{-9} to control the growth of the bond dimension D, which reaches maximum values of approximately 1000 in the most challenging setting. Additionally, for calculating the meson numbers defined in Eq. (23), we use a larger cutoff of 10^{-8}, because we need to calculate the expectation of nonlocal operators in the state with large bond dimension after the collision.

Within TEBD, the time-evolution operator is approximated by a second-order Trotter decomposition,

$$e^{-iHt} \approx \left(e^{-iH_{\text{odd}}\ \frac{\Delta t}{2}} e^{-iH_{\text{even}}\ \Delta t} e^{-iH_{\text{odd}}\ \frac{\Delta t}{2}}\right)^{t/\Delta t}, \tag{E2}$$

where Δt is the time step and $e^{-iH_{\text{even}}\ \Delta t}$ ($e^{-iH_{\text{odd}}\ \Delta t}$) represents the Hamiltonian terms starting at even (odd) matter sites given by

$$e^{-iH_{\text{even}}\ \Delta t} = \prod_{n\in\text{even}} e^{-iH_n \Delta t} \tag{E3}$$

for even sites and analogously for the odd sites. Specifically for $n < L$, H_n reads

$$\begin{aligned} H_n = &-\frac{i}{2a}(\sigma_n^+ Z_{g,n}\sigma_{n+1}^- - \text{H.c.}) \\ &+ \frac{m}{4}(-1)^n\left(\sigma_n^z - \sigma_{n+1}^z\right) + \varepsilon X_{g,n}, \end{aligned} \tag{E4}$$

and for $n = L$:

$$\begin{aligned} H_L = &\frac{1}{2a}\left(\prod_{l<L}\left(-i\sigma_l^z\right)\sigma_L^+ Z_{g,L}\sigma_1^- + \text{H.c.}\right) \\ &+ \frac{m}{4}(-1)^L\left(\sigma_L^z - \sigma_1^z\right) + \varepsilon X_{g,L}, \end{aligned} \tag{E5}$$

which takes into account the periodic boundary conditions. We employ TEBD here as a straightforward implementation; alternative MPS time-evolution algorithms such as the time-dependent variational principle may require smaller bond dimensions for comparable accuracy, and represent a natural option for extending the simulations further.

APPENDIX F: EFFECT OF MOMENTUM TRUNCATION ON THE SCATTERING DYNAMICS

In the QSE-based initial-state construction, the meson operator is expanded in a finite set of momentum modes. As discussed in Sec. IV, for $(m, \varepsilon) = (0.1, 0.2)$, the maximum momentum we got for the vector meson is $|k| \leqslant 9 \times (2\pi/L)$, the systematic uncertainty arises from the truncation of this momentum sum. To examine the robustness of the inelastic features reported in the main text, we use setup $(m, \varepsilon) = (0.2, 0.2)$ to analyze the effect of momentum truncation. The momentum window we got for vector meson in this setup is $|k| \leqslant 10 \times (2\pi/L)$, and the weight of the discarded momenta beyond this window is very small,

$$\sum_{|k|>10(2\pi/L)} |\phi(k)|^2 \approx 0.0045, \tag{F1}$$

where $\phi(k)$ is the normalized Gaussian profile used to construct the incoming wave packet. We use this result as reference and shrink the momentum window to $|k| \leqslant 9 \times (2\pi/L)$ to analyze the truncation effect.

Figure 18 compares the original and extended-truncation simulations for $(m, \varepsilon) = (0.2, 0.2)$ at $L = 30$. The fermion density and electric field density in the scattering process remain qualitatively unchanged upon including the higher-momentum modes. The characteristic inelastic features are preserved in the extended analysis. The only visible modification is a modest suppression of the two vector meson channel and enhancement of two scalar meson channel, which is consistent with the inclusion of energetically higher components in the initial wave packet.

We further compare the time-dependent energy transfer and the meson density extracted from the two truncations. These quantities are consistent throughout the evolution, confirming that the scattering dynamics are stable against reasonable enlargements of the momentum window.

Taken together, these observations demonstrate that the inelastic signatures, including $(m, \varepsilon) = (0.1, 0.2)$ reported in the main text, are physical effects, rather than artifacts of the momentum truncation.

APPENDIX G: OPERATOR POOL REDUCTION VIA TRANSLATION INVARIANCE

In Sec. III, we construct the QSE operator pool from the full set of fermion bilinears $\{M_I = \xi_n^\dagger W_{n,l}\xi_l \,|\, I = (n, l)\}$, of size $\mathcal{O}(L^2)$, and solve simultaneously for all momentum modes. When only a specific momentum mode is required, translation invariance allows for a significant reduction of the operator pool.

For a target momentum k and charge-conjugation eigenvalue c, the operator pool can be restricted to translationally invariant combinations labeled by the Wilson-line displace-

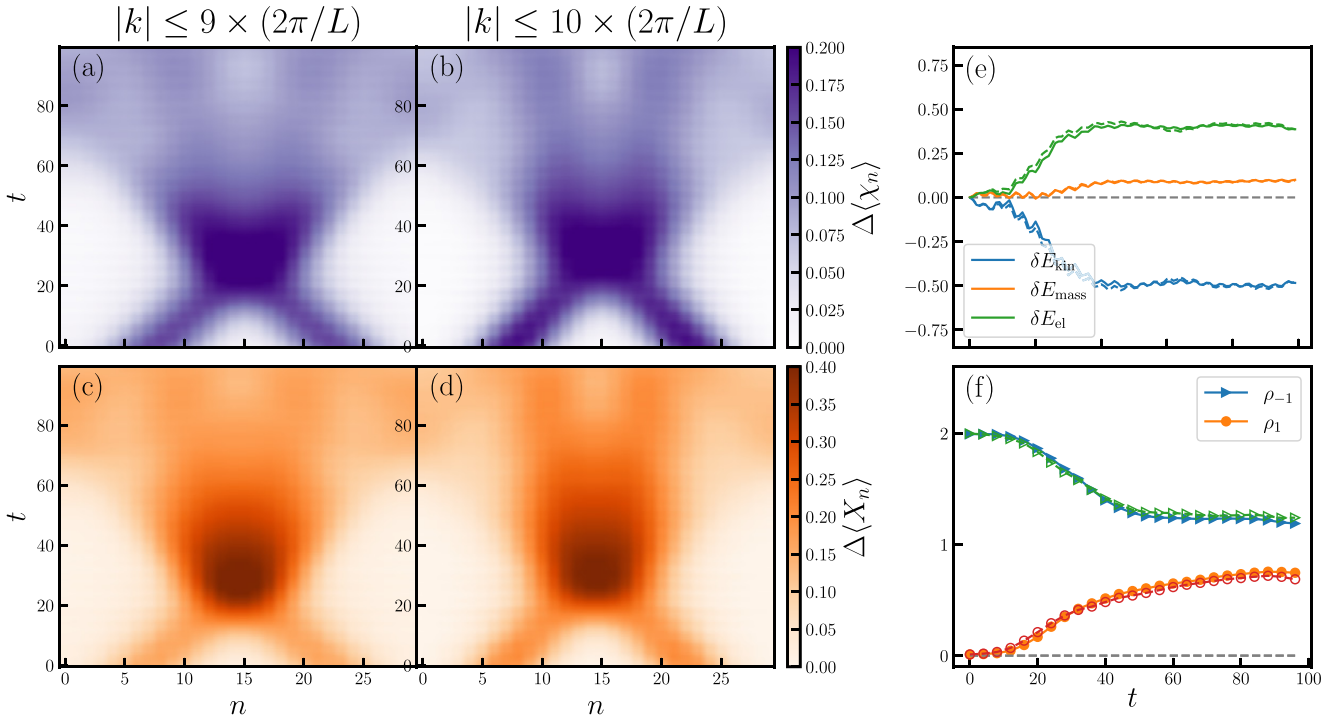

FIG. 18. Comparison of the different momentum truncation results for $(m, \varepsilon) = (0.2, 0.2)$ at $L = 30$. Left: Original results with $|k| \leqslant 9 \times (2\pi/L)$, showing (a) fermion density and (c) electric field. Middle: Extended results with $|k| \leqslant 10 \times (2\pi/L)$, shown in panels (b) and (d). Right: Energy transfer [panel (e)] and meson density [panel (f)]; dashed (empty symbols) and solid (filled symbols) curves correspond to $|k| \leqslant 9 \times (2\pi/L)$ and $|k| \leqslant 10 \times (2\pi/L)$, respectively.

ment d alone:

$$M_e^d(k,c) = \sum_{n\in\text{even}} e^{-ikn}\xi_n^\dagger\xi_{n+d} + c(-1)^{d+1}\sum_{n\in\text{odd}} e^{-ikn}\xi_{n+d}^\dagger\xi_n,$$
$$M_o^d(k,c) = \sum_{n\in\text{odd}} e^{-ikn}\xi_n^\dagger\xi_{n+d} + c(-1)^{d+1}\sum_{n\in\text{even}} e^{-ikn}\xi_{n+d}^\dagger\xi_n. \tag{G1}$$

The even- and odd-site contributions are treated separately in order to respect the two-site translational symmetry of staggered fermions and to ensure correct transformation properties under charge conjugation. If the maximum Wilson-line length is restricted to D, the operator pool in a single (k, c) sector has dimension $2D$, independent of the system size L. Solving the QSE independently for each momentum mode k in this reduced pool is therefore typically more efficient than constructing the full $\mathcal{O}(L^2)$ pool and solving for all momenta simultaneously, since the cost of computing the relevant matrix elements scales polynomially in D alone in the per-momentum approach.

[1] O. Brüning, H. Burkhardt, and S. Myers, The large hadron collider, Prog. Part. Nucl. Phys. **67**, 705 (2012).

[2] S. Dürr, Z. Fodor, J. Frison, C. Hoelbling, R. Hoffmann, S. D. Katz, S. Krieg, T. Kurth, L. Lellouch, T. Lippert, K. K. Szabo, and G. Vulvert, *Ab initio* determination of light hadron masses, Science **322**, 1224 (2008).

[3] C. Alexandrou, Hadron properties from lattice QCD, J. Phys.: Conf. Ser. **562**, 012007 (2014).

[4] Y. Aoki *et al.*, Flag review 2024, Phys. Rev. D **113**, 014508 (2026).

[5] Z. Davoudi, W. Detmold, P. Shanahan, K. Orginos, A. Parreño, M. J. Savage, and M. L. Wagman, Nuclear matrix elements from lattice QCD for electroweak and beyond-Standard-Model processes, Phys. Rep. **900**, 1 (2021).

[6] M. Constantinou *et al.*, Parton distributions and lattice-QCD calculations: Toward 3D structure, Prog. Part. Nucl. Phys. **121**, 103908 (2021).

[7] G. Pan and Z. Y. Meng, The sign problem in quantum Monte Carlo simulations, in *Encyclopedia of Condensed Matter Physics*, edited by T. Chakraborty, 2nd ed. (Academic Press, Oxford, 2024), pp. 879–893.

[8] M. C. Bañuls, K. Cichy, J. I. Cirac, K. Jansen, and S. Kühn, Tensor networks and their use for lattice gauge theories, PoS **(LATTICE 2018)**, 022 (2019).

[9] M. C. Bañuls and K. Cichy, Review on novel methods for lattice gauge theories, Rep. Prog. Phys. **83**, 024401 (2020).

[10] P. Silvi, E. Rico, M. Dalmonte, F. Tschirsich, and S. Montangero, Finite-density phase diagram of a (1+1)-*d* non-Abelian lattice gauge theory with tensor networks, Quantum **1**, 9 (2017).

[11] G. Magnifico, T. Felser, P. Silvi, and S. Montangero, Lattice quantum electrodynamics in (3+1)-dimensions at finite density with tensor networks, Nat. Commun. **12**, 3600 (2021).

[12] T. Angelides, L. Funcke, K. Jansen, and S. Kühn, Computing the mass shift of Wilson and staggered fermions in the lattice

Schwinger model with matrix product states, Phys. Rev. D **108**, 014516 (2023).
[13] R. G. Jha, A. Milsted, D. Neuenfeld, J. Preskill, and P. Vieira, Real-time scattering in Ising field theory using matrix product states, Phys. Rev. Res. **7**, 023266 (2025).
[14] I. Papaefstathiou, J. Knolle, and M. C. Bañuls, Real-time scattering in the lattice Schwinger model, Phys. Rev. D **111**, 014504 (2025).
[15] J. C. Halimeh, N. Mueller, J. Knolle, Z. Papić, and Z. Davoudi, Quantum simulation of out-of-equilibrium dynamics in gauge theories, arXiv:2509.03586.
[16] P. Calabrese and J. Cardy, Evolution of entanglement entropy in one-dimensional systems, J. Stat. Mech. (2005) P04010.
[17] N. Schuch, M. M. Wolf, F. Verstraete, and J. I. Cirac, Entropy scaling and simulability by matrix product states, Phys. Rev. Lett. **100**, 030504 (2008).
[18] J. Schachenmayer, B. P. Lanyon, C. F. Roos, and A. J. Daley, Entanglement growth in quench dynamics with variable range interactions, Phys. Rev. X **3**, 031015 (2013).
[19] M. Rigobello, S. Notarnicola, G. Magnifico, and S. Montangero, Entanglement generation in $(1+1)$D QED scattering processes, Phys. Rev. D **104**, 114501 (2021).
[20] E. A. Martinez, C. A. Muschik, P. Schindler, D. Nigg, A. Erhard, M. Heyl, P. Hauke, M. Dalmonte, T. Monz, P. Zoller, and R. Blatt, Real-time dynamics of lattice gauge theories with a few-qubit quantum computer, Nature (London) **534**, 516 (2016).
[21] N. Klco, E. F. Dumitrescu, A. J. McCaskey, T. D. Morris, R. C. Pooser, M. Sanz, E. Solano, P. Lougovski, and M. J. Savage, Quantum-classical computation of Schwinger model dynamics using quantum computers, Phys. Rev. A **98**, 032331 (2018).
[22] Y. Y. Atas, J. F. Haase, J. Zhang, V. Wei, S. M.-L. Pfaendler, R. Lewis, and C. A. Muschik, Simulating one-dimensional quantum chromodynamics on a quantum computer: Real-time evolutions of tetra- and pentaquarks, Phys. Rev. Res. **5**, 033184 (2023).
[23] F. M. Surace and A. Lerose, Scattering of mesons in quantum simulators, New J. Phys. **23**, 062001 (2021).
[24] G.-X. Su, J. J. Osborne, and J. C. Halimeh, Cold-atom particle collider, PRX Quantum **5**, 040310 (2024).
[25] R. C. Farrell, M. Illa, A. N. Ciavarella, and M. J. Savage, Quantum simulations of hadron dynamics in the Schwinger model using 112 qubits, Phys. Rev. D **109**, 114510 (2024).
[26] Y. Chai, A. Crippa, K. Jansen, S. Kühn, V. R. Pascuzzi, F. Tacchino, and I. Tavernelli, Fermionic wave packet scattering: A quantum computing approach, Quantum **9**, 1638 (2025).
[27] C. Alexandrou, A. Athenodorou, K. Blekos, G. Polykratis, and S. Kühn, Realizing string breaking dynamics in a $\mathbb{Z}_2$ lattice gauge theory on quantum hardware, Phys. Rev. D **112**, 114506 (2025).
[28] E. J. Gustafson and H. Lamm, Toward quantum simulations of $\mathbb{z}_2$ gauge theory without state preparation, Phys. Rev. D **103**, 054507 (2021).
[29] J. Mildenberger, W. Mruczkiewicz, J. C. Halimeh, Z. Jiang, and P. Hauke, Confinement in a $\mathbb{Z}_2$ lattice gauge theory on a quantum computer, Nat. Phys. **21**, 312 (2025).
[30] Z.-Y. Zhou, G.-X. Su, J. C. Halimeh, R. Ott, H. Sun, P. Hauke, B. Yang, Z.-S. Yuan, J. Berges, and J.-W. Pan, Thermalization dynamics of a gauge theory on a quantum simulator, Science **377**, 311 (2022).
[31] R. C. Farrell, M. Illa, A. N. Ciavarella, and M. J. Savage, Scalable circuits for preparing ground states on digital quantum computers: The Schwinger model vacuum on 100 qubits, PRX Quantum **5**, 020315 (2024).
[32] R. C. Farrell, N. A. Zemlevskiy, M. Illa, and J. Preskill, Digital quantum simulations of scattering in quantum field theories using W states, arXiv:2505.03111.
[33] N. A. Zemlevskiy, Scalable quantum simulations of scattering in scalar field theory on 120 qubits, Phys. Rev. D **112**, 034502 (2025).
[34] Z. Davoudi, C.-C. Hsieh, and S. V. Kadam, Scattering wave packets of hadrons in gauge theories: Preparation on a quantum computer, Quantum **8**, 1520 (2024).
[35] Z. Davoudi, A. F. Shaw, and J. R. Stryker, General quantum algorithms for Hamiltonian simulation with applications to a non-Abelian lattice gauge theory, Quantum **7**, 1213 (2023).
[36] D. Horn, M. Weinstein, and S. Yankielowicz, Hamiltonian approach to $Z(N)$ lattice gauge theories, Phys. Rev. D **19**, 3715 (1979).
[37] J. Kogut and L. Susskind, Hamiltonian formulation of Wilson's lattice gauge theories, Phys. Rev. D **11**, 395 (1975).
[38] L. Susskind, Lattice fermions, Phys. Rev. D **16**, 3031 (1977).
[39] M. Carena, Y.-Y. Li, T. Ou, and H. Singh, Real-time simulation of asymmetry generation in fermion-bubble collisions, Phys. Rev. D **113**, 014502 (2026).
[40] M. Stone, Gamma matrices, Majorana fermions, and discrete symmetries in Minkowski and Euclidean signature, J. Phys. A: Math. Theor. **55**, 205401 (2022).
[41] The operator C used here corresponds to C_- in Ref. [39]. The fermion field ξ_n differs from χ_n used in that work by a phase factor, leading to a slightly different form of the transformation in Eq. (3) compared to Eq. (A11) in Ref. [39], though the underlying physics is the same.
[42] S. Coleman, More about the massive Schwinger model, Ann. Phys. **101**, 239 (1976).
[43] M. C. Bañuls, K. Cichy, J.I. Cirac, and K. Jansen, The mass spectrum of the Schwinger model with matrix product states, J. High Energy Phys. 11 (2013) 158.
[44] E. R. Anschuetz and B. T. Kiani, Quantum variational algorithms are swamped with traps, Nat. Commun. **13**, 7760 (2022).
[45] M. Larocca, S. Thanasilp, S. Wang, K. Sharma, J. Biamonte, P. J. Coles, L. Cincio, J. R. McClean, Z. Holmes, and M. Cerezo, Barren plateaus in variational quantum computing, Nat. Rev. Phys. **7**, 174 (2025).
[46] G. Scriva, N. Astrakhantsev, S. Pilati, and G. Mazzola, Challenges of variational quantum optimization with measurement shot noise, Phys. Rev. A **109**, 032408 (2024).
[47] J. R. McClean, M. E. Kimchi-Schwartz, J. Carter, and W. A. de Jong, Hybrid quantum-classical hierarchy for mitigation of decoherence and determination of excited states, Phys. Rev. A **95**, 042308 (2017).
[48] J. R. McClean, Z. Jiang, N. C. Rubin, R. Babbush, and H. Neven, Decoding quantum errors with subspace expansions, Nat. Commun. **11**, 636 (2020).
[49] T. Takeshita, N. C. Rubin, Z. Jiang, E. Lee, R. Babbush, and J. R. McClean, Increasing the representation accuracy of quan-

tum simulations of chemistry without extra quantum resources, Phys. Rev. X **10**, 011004 (2020).
[50] N. Yoshioka, T. Sato, Y. O. Nakagawa, Y.-Y. Ohnishi, and W. Mizukami, Variational quantum simulation for periodic materials, Phys. Rev. Res. **4**, 013052 (2022).
[51] Each of the operators in the expectation value can be expressed as matrix product operator with constant bond dimension. Hence, the cost of contracting the resulting network scales linearly in L and the computation is efficient.
[52] M. Fishman, S. R. White, and E. M. Stoudenmire, Codebase release 0.3 for ITensor, SciPost Phys. Codebases 4-r0.3 (2022).
[53] Including two more excited states for $(m, \varepsilon) = (0.1, 0.2)$ only adds higher scalar excitations rather than higher-momentum vector modes, and thus does not enlarge the relevant momentum window. For consistency, we retain the 28 state basis for $(m, \varepsilon) = (0.1, 0.2)$.
[54] S. P. Jordan, K. S. M. Lee, and J. Preskill, Quantum algorithms for quantum field theories, Science **336**, 1130 (2012).
[55] S. P. Jordan, K. S. M. Lee, and J. Preskill, Quantum computation of scattering in scalar quantum field theories, Quantum Inf. Comput. **14**, 1014 (2014).
[56] A. Peruzzo, J. McClean, P. Shadbolt, M.-H. Yung, X.-Q. Zhou, P. J. Love, A. Aspuru-Guzik, and J. L. O'Brien, A variational eigenvalue solver on a photonic quantum processor, Nat. Commun. **5**, 4213 (2014).
[57] X. Yuan, S. Endo, Q. Zhao, Y. Li, and S. C. Benjamin, Theory of variational quantum simulation, Quantum **3**, 191 (2019).
[58] J. Gacon, J. Nys, R. Rossi, S. Woerner, and G. Carleo, Variational quantum time evolution without the quantum geometric tensor, Phys. Rev. Res. **6**, 013143 (2024).
[59] D. Wecker, M. B. Hastings, N. Wiebe, B. K. Clark, C. Nayak, and M. Troyer, Solving strongly correlated electron models on a quantum computer, Phys. Rev. A **92**, 062318 (2015).
[60] I. D. Kivlichan, J. McClean, N. Wiebe, C. Gidney, A. Aspuru-Guzik, G. K.-L. Chan, and R. Babbush, Quantum simulation of electronic structure with linear depth and connectivity, Phys. Rev. Lett. **120**, 110501 (2018).
[61] Z. Jiang, K. J. Sung, K. Kechedzhi, V. N. Smelyanskiy, and S. Boixo, Quantum algorithms to simulate many-body physics of correlated fermions, Phys. Rev. Appl. **9**, 044036 (2018).
[62] Note that $R^{\dagger}_{nl}(\theta, \tilde{\xi})$ would correspond to $V^{\dagger}(r_{n,l})$ in the second line of Eq. (44) in Ref. [26].
[63] For our purposes, the explicit form of u_a is not of importance. We are concerned solely with the existence of a unitary matrix u_a whose first column has the aforementioned entries. The remaining columns can be constructed to ensure that u_a is unitary, for example, by applying the Gram-Schmidt orthonormalization process.
[64] L. Viola and S. Lloyd, Dynamical suppression of decoherence in two-state quantum systems, Phys. Rev. A **58**, 2733 (1998).
[65] P. Krantz, M. Kjaergaard, F. Yan, T. P. Orlando, S. Gustavsson, and W. D. Oliver, A quantum engineer's guide to superconducting qubits, Appl. Phys. Rev. **6**, 021318 (2019).
[66] J. Schuhmacher, G.-X. Su, J. J. Osborne, A. Gandon, J. C. Halimeh, and I. Tavernelli, Observation of hadron scattering in a lattice gauge theory on a quantum computer, arXiv:2505.20387.
[67] Z. Davoudi, C.-C. Hsieh, and S. V. Kadam, Quantum computation of hadron scattering in a lattice gauge theory, arXiv:2505.20408.
[68] N. Yoshioka, H. Hakoshima, Y. Matsuzaki, Y. Tokunaga, Y. Suzuki, and S. Endo, Generalized quantum subspace expansion, Phys. Rev. Lett. **129**, 020502 (2022).
[69] W. Ritz, Über eine neue methode zur lösung gewisser variationsprobleme der mathematischen physik, J. Angew. Math. **135**, 1 (1909).
[70] U. Schollwöck, The density-matrix renormalization group in the age of matrix product states, Ann. Phys. **326**, 96 (2011).
[71] R. Orús, A practical introduction to tensor networks: Matrix product states and projected entangled pair states, Ann. Phys. **349**, 117 (2014).
[72] M. C. Bañuls, Tensor network algorithms: A route map, Annu. Rev. Condens. Matter Phys. **14**, 173 (2023).